Politecnico
di Torino

Politecnico di Torino

MS in Mathematical Engineering

Steam Generator Tube Rupture accident scenario in Lead Fast Reactor: assessment of numerical modelling for shock wave generation and propagation

Candidate: Lorenza Egle Bonfanti Posta

Supervisors: Prof. Domenic D'Ambrosio
Dr. Gabriele Ottino (Newcleo S.p.A.)

Academic Year 2024/25

Acknowledgements

I would like to thank Newcleo S.p.A. for giving me the opportunity to conduct my thesis research in its Codes and Methods department, Codes Development unit, from 10 March to 30 September 2025.

Abstract

In Lead-cooled Fast Reactors (LFRs), a type of Gen-IV nuclear reactor, the limited chemical reactivity between water and lead allows for innovative designs in which the primary circuit, comprising of high-temperature molten lead pool, and the secondary circuit, containing the steam generator with high-pressure subcooled water, are placed in direct contact. Although this configuration offers several technological and thermodynamic advantages, it also introduces a new potential accident scenario, known as Steam Generator Tube Rupture (SGTR). An SGTR occurs when a tube in the secondary circuit breaks within the molten lead pool. The consequences of this accident have not yet been fully characterized in the scientific literature. However, it is already known that the initial effect of such an event is the propagation of a shock wave through the molten lead pool, caused by the significant pressure difference between the two fluids in contact. Since the management of all possible accident scenarios is required for the safety evaluations of nuclear reactor designs, the SGTR event must be thoroughly assessed in the coming years. In the absence of experimental data, numerical simulations are currently the most effective tool for supporting safety analysis. This study implements and applies two models available in the literature to reconstruct and analyse the evolution of the flow field in an SGTR scenario. The first model is a 3D shock propagation model involving two distinct compressible fluids, that is, a water-vapour mixture at saturated conditions and molten lead. Spherical symmetry is assumed. The governing Euler-type equations are the same for both fluids; the equations of state, however, are specific to each fluid. These equations are discretised using the finite volume method, and an Osher solver is adopted to calculate interface fluxes and perform time integration. The level-set method is employed to track the motion of the water-lead interface over time, and a ghost fluid method is implemented to address multi-material interactions during time integration. The second model is presented in the literature as a simplified version of the first. Since the involved velocities in the lead are largely subsonic, the lead is modelled as an incompressible fluid. Additionally, the physical properties of the water are described as volume-averaged. These assumptions result in a simplified model that is useful for describing the evolution of the water–lead interface over time. The entire model is derived as a system of ordinary differential equations (ODEs), which describes the evolution of the water-lead interface in terms of its radial coordinate, velocity, and pressure. Then, by exploiting the continuity of pressure and velocity across the interface, the physical quantities of the lead (radial velocity and pressure) can also be obtained. A comparison is provided between the results from the literature and both model outcomes, in order to verify the correctness of the calculations. This is also necessary because the mathematical methods adopted differ from those in the reference papers. Thorough analyses are then performed and described.

Contents

List of Figures

1 Introduction

In Lead-cooled Fast Reactors (LFRs), a type of Gen-IV nuclear reactor, the chemical inertia between water and lead allows for innovative designs. The primary circuit, which is represented by a high-temperature molten lead pool, is in direct contact with the secondary circuit, which consists of a steam generator with high-pressure subcooled water. Although this configuration offers several technological and thermodynamic advantages, it also introduces a new potential accident scenario, known as Steam Generator Tube Rupture (SGTR).
An SGTR occurs when a tube in the secondary circuit breaks within the molten lead pool. A scheme of the accident scenario is reported in Fig. 1.
The consequences of this accident have not yet been fully characterised in the scientific literature. However, a preliminary classification is reported in [1]. The main phenomena associated with an SGTR scenario include shock wave propagation, sloshing, a form of steam detonation (known as CCI) and core voiding, a neutronic consequence caused by vapor bubble transport to the reactor core. The pressure discontinuity is believed to trigger all the other phenomena, and then its short-term consequences have been the focus of this thesis work.
To conduct experimental investigations on the SGTR scenario, some facilities have been built, such as those reported in [2]. However, this data is currently not enough to permit a deep insight about the SGTR outcomes, thus computer codes such as SIMMER [3] and EUROPLEXUS [4], have been used to support research studies. Although useful, these codes focus on fast dynamics and none of those investigate the initializing phenomenon: this subject has been addressed in literature through the proposal of some dedicated models.
In [5] and [6] two analytical models are presented to investigate shock propagation and the evolution of the water-lead interface time. These two models have been implemented during this thesis work. In addition, some analytical models are provided in [7], [8] and [9] focusing on the CCI steam explosion that has been defined for the first time in [10] as an extreme increase of pressure due to the thermal reaction between two materials (i.e., molten lead and liquid water).

As mentioned above, the thesis focuses on two models that describe the SGTR initiating phenomena.
The first model is a one dimensional, spherically symmetric shock-propagation model involving two distinct compressible fluids, that is, water-vapour mixture at saturated conditions and molten lead. Spherical symmetry is assumed, as the blowout of secondary circuit tube is approximated as a droplet. The governing equations are the mass and momentum conservation equations for inviscid fluids, without diffusive terms; the equations of state are specific to each fluid. These equations are discretized using the finite volume method, and an Osher solver is adopted to calculate interface fluxes. The integration in time is performed using a first-order backward Euler scheme. The level-set method is employed to track the motion of the water-lead interface over time, and a ghost fluid method is implemented to handle multi-material interactions in time following the approach described in [11].
The second model represents a simplified formulation of the first. Since the involved velocities in the lead are largely subsonic, the lead is modeled as an incompressible fluid. This assumption is useful to quickly reproduce the evolution of the

water–lead interface over time. The entire model results in a system of ordinary differential equations (ODEs), which describes the evolution of the water-lead interface in terms of its radial coordinate, velocity, and pressure.
The calculations' correctness is verified by comparing the results from the literature with those of the models.
Finally, both physical and numerical analysis of the obtained results are provided, together with a grid convergence study for the first model.

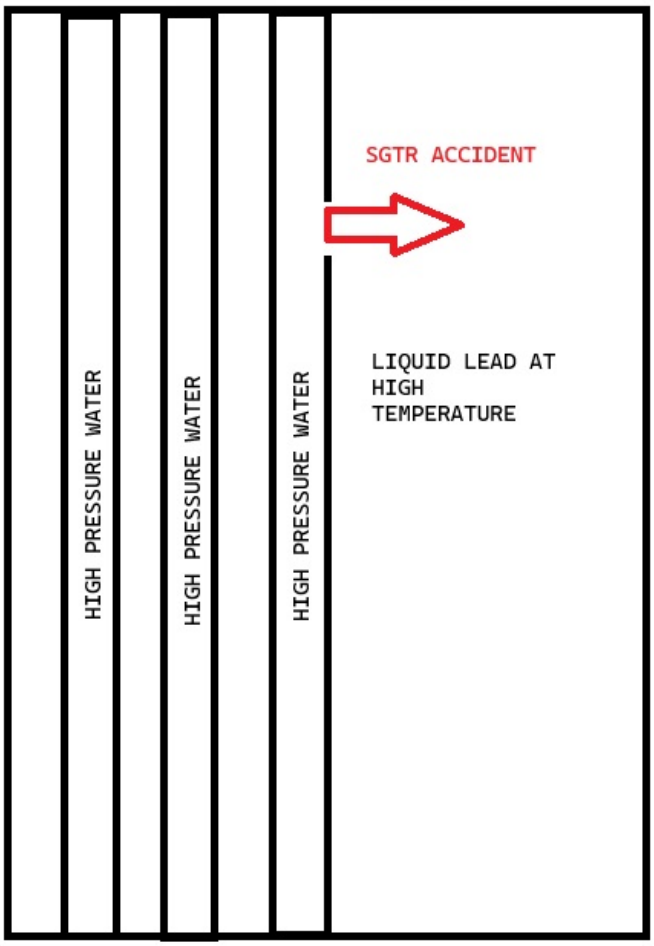

Figure 1: SGTR scenario scheme.

2 Phenomenology

It is important to note that a complete description of the SGTR consequences is still unavailable and remains an active subject of research; nevertheless, an assessment of the main SGTR phenomena has been presented by T. Dinh in [1], which provides a classification of the principal phenomena that should be considered as a starting point for further investigation.

The categorization proposed in [1] is as follows:

- **Initial shock wave:** This phenomenon occurs due to the pressure discontinuity between high-pressure water in the secondary circuit and high-temperature molten lead in the primary circuit. It is characterized by wave propagation, reflection and interaction processes.
- **Sloshing**: This occurs as a result of water evaporation and the expansion of steam bubble into the lead environment. It must be considered when evaluating the mechanical stress on the reactor walls.
- **Coolant–Coolant Interaction (CCI):** A specific type of steam explosion can occur if the steam generator leaks in an area where water remains in its liquid state. The contact between high-temperature molten lead and liquid water may result in a strong pressure increase caused by complex thermodynamic interactions. A detailed description is provided in [8] and [9]. However, [1] also presents several considerations suggesting that this particular consequence is unlikely:
  - The time window for CCI to occur is short, since the evaporation time of liquid water has been estimated to be on the order of one minute.
  - The liquid water is expected to be surrounded by a thick vapor film that prevents effective contact between molten lead and liquid water.
  - The surface tension and density of molten lead are about one order of magnitude higher than those of water, which suppresses the development of short-wavelength instabilities in small vapor bubbles.
  - The finite discharge rate from the failure site limits the amount of liquid water present in the lead pool during the event.
- **Core voiding:** This is presented as a possible neutronic consequence of SGTR, since the transport of steam bubbles toward the reactor core can have significant effects. Although this stage of the accident is of interest, it involves neutronic phenomena and has therefore not been examined in detail in the present work.

In the secondary circuit, the main issues are blowout and depressurization. [1] The following sections describe the mathematical models considered to simulate the initiating thermodynamic phenomena.

3 Initial Shock Wave - Shock Impact Model

The initial time $t = 0$ s is defined as the instant at which the tube rupture occurs. The pressure difference between the primary and secondary circuits immediately induces the propagation of a shock wave. This phenomenon has been modeled following the approach proposed in [5] and [6].

3.1 Problem formulation

Consider a single water droplet under initial saturation conditions defined by $p_{w,0}$ and $T_{w,0}$. At time $t = 0$, the droplet comes into contact with molten lead, characterized by a higher temperature, $T_{l,0}$, and a lower pressure, $p_{l,0}$, with respect to water. These conditions cause a compression wave to propagate through the molten lead and a rarefaction wave to propagate within the water droplet. A phase change in the water occurs, although the water is supposed to remain at saturation conditions. A schematic representation of the multiphase flow configuration is shown in Fig. 2.

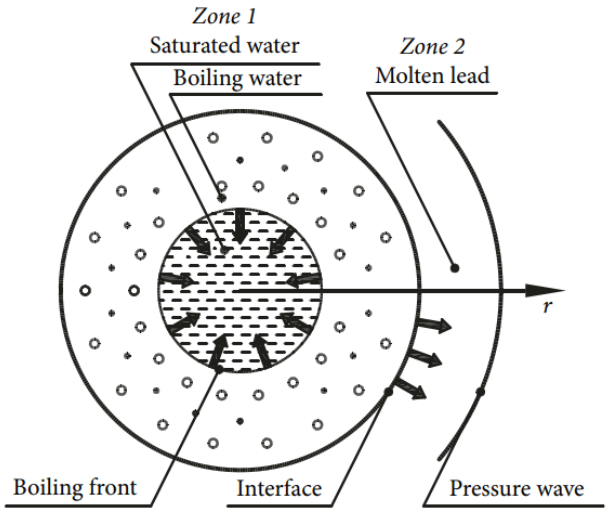

Figure 2: Schematic representation of the main zones for the expansion of superheated water into liquid coolant [5].

The main assumptions of this model are as follows:

- Since the study focuses on a droplet, spherical symmetry is assumed;
- In *Zone* 1 (water domain), thermodynamic equilibrium between liquid water and vapor is assumed, meaning that interfacial processes are considered fast enough to maintain the interface on the saturation line. The mixture is also assumed to behave isentropically;
- In *Zone* 2 (molten lead domain), lead is treated as an inviscid, compressible fluid.

3.2 Mathematical modeling

The following section provides the mathematical description of the water and lead domains, together with the formulation of interface conditions between the two

materials .

3.2.1 Water Zone

Based on the above assumptions, the water can be described as a homogeneous mixture rather than as two distinct phases. The mixture quantities are denoted by the subscript w. Let ρ_w, p_w and u_w represent the mixture density, pressure, and velocity, respectively. The governing equations are:

$$\frac{\partial \rho_w}{\partial t} + \frac{1}{r^2}\frac{\partial(\rho_w u_w r^2)}{\partial r} = 0; \tag{1}$$

$$\frac{\partial(\rho_w u_w)}{\partial t} + \frac{1}{r^2}\frac{\partial(\rho_w u_w^2 r^2)}{\partial r} = -\frac{\partial p_w}{\partial r}. \tag{2}$$

Equations 1 and 2 are closed by the two-phase equation of state:

$$\rho_w = \frac{1}{(1-\chi_v(p_w))\nu_{s,l}(p_w) + \chi_v(p_w)\nu_{s,v}(p_w)}; \tag{3}$$

where:

- $\nu_{s,v}$ is the specific volume of the vapor phase;
- $\nu_{s,l}$ is the specific volume of the liquid phase;
- χ_v is the vapor mass fraction, defined as:

$$\chi_v(p_w, p_{w,0}) = \frac{s_{w,0}(p_{w,0}) - s_{s,l}(p_w)}{s_{s,v}(p_w) - s_{s,l}(p_w)}, \tag{4}$$

where $s_{w,0}(p_{w,0})$ is the initial specific entropy, $s_{s,v}(p_w)$ is the saturated vapor entropy and $s_{s,l}(p_w)$ is the saturated liquid entropy.

Under the assumption of thermodynamic equilibrium, all thermodynamic quantities in Zone 1 depend only on p_w, allowing the flow to be considered as barotropic. It is also important to note that, due to the saturation condition assumption, the energy conservation equation is not included in the governing equations system.

3.2.2 Lead zone

In the molten lead domain ($Zone\,2$), physical quantities are denoted by the subscript l. The governing equations are similar to those of water:

$$\frac{\partial \rho_l}{\partial t} + \frac{1}{r^2}\frac{\partial(\rho_l u_l r^2)}{\partial r} = 0; \tag{5}$$

$$\frac{\partial(\rho_l u_l)}{\partial t} + \frac{1}{r^2}\frac{\partial(\rho_l u_l^2 r^2)}{\partial r} = -\frac{\partial p_l}{\partial r}. \tag{6}$$

To close the lead system, the Tait equation of state is adopted:

$$p_l = p_* + B\left[\left(\frac{\rho_l}{\rho_*}\right)^{\gamma} - 1\right], \tag{7}$$

where starred quantities denote reference values for lead, and γ and B are material-specific parameters. As in the water domain, the flow is assumed to be barotropic, since the phenomenon occurs over time scales too short for significant heat exchange.

3.2.3 Water-lead interface

The two domains are separated by a contact surface characterized by a discontinuity in density. The interaction between the two media can be described using the method of characteristics, as follows:

$$\begin{cases} u_I = u_w - \int_{p_w}^{p_I} \frac{dp}{\rho_w c_w} \\ u_I = u_l + \int_{p_l}^{p_I} \frac{dp}{\rho_l c_l} \end{cases} \tag{8}$$

where u_I and p_I characterize the interface, and c_w and c_l are the sound speeds in water and lead, respectively.

3.3 Implementation

The above model was implemented, and the results were compared with those reported in [5] and [6]. Instead of the HR-SLAU2 method proposed in [5], the chosen numerical approach was an Osher solver, which is described below.

3.3.1 Initial and boundary conditions

Since the flow is barotropic, the only initial condition required is the pressure distribution, defined as:

$$\begin{cases} p = p_{w,0} & r < R_{w,0} \\ p = p_{l,0} & otherwhise \end{cases} \tag{9}$$

Here, $R_{w,0}$ is the initial radius of the all-liquid water droplet. Both water and molten lead are assumed to be motionless at the initial time, as any other condition would be inconsistent with the assumption of spherical symmetry.

The boundary conditions are set as follows:

- **Inlet:** The velocity at $r = 0$ is set to zero due to spherical symmetry;
- **Outlet:** Three possible configurations are considered to apply the appropriate boundary conditions:
  - If the end of the domain remains unaffected by shock propagation (i.e. its initial state does not change during the simulation), the pressure and velocity at the boundary are set equal to those in the last cell.
  - If the flow reaches the domain boundary and is supersonic, no outlet condition is required.
  - If the flow reaches the domain boundary and is subsonic, the simulation is stopped, since valid boundary conditions cannot be imposed.

3.3.2 Substance properties - Water mixture

The equation of state (EoS) for water relates the pressure and density through entropy and specific volume. The quantities $\nu_{s,v}$, $\nu_{s,l}$, $s_{s,l}$, and $s_{s,v}$ are pressure dependent, and their functional relationships are not explicitly defined. Therefore, a linear interpolation was performed on NIST tabulated data for saturated water [12]. Pressure values were sampled in the range 1–22 MPa with a 0.1 MPa increment. The speed of sound was calculated using the definition:

$$c_w = \sqrt{\frac{\partial p_w}{\partial \rho_w}}_{S=cost} \tag{10}$$

3.3.3 Substance properties - Lead

The Tait equation of state requires two parameters to be estimated. By equating the initial speed of sound obtained by the NEA correlation [13] with that derived from the Tait equation (assuming the starred quantities are equal to initial ones), the following relation is obtained:

$$c_l = 1953 - 0.246T_0 = \sqrt{\frac{\partial p_{l,0}}{\partial \rho_{l,0}}}_{S=cost} = \sqrt{B\gamma \frac{\rho_{l,0}^{\gamma-1}}{\rho_*^{\gamma}}} = 1756\, m/s \tag{11}$$

where $T_0 = 800\, K$.
From this relation, it is possible to estimate $B\gamma = 3.212\, MPa$. By linearizing the equation, it can be observed that, within the considered pressure range of 1-22 MPa, the sensitivity to the Tait equation parameters is very low. The selected parameter values are $B = 2677.5 MPa$ and $\gamma = 12$.

3.4 Numerical solver

To solve the governing system of equations, a dedicated numerical solver was implemented. The mathematical formulation of the solver is described below. A first-order spatial reconstruction was adopted: results are reported for a uniform mesh of 10000 elements in a $0.5\, m$ radial domain.

3.4.1 Finite Volume Method (FVM)

The computational domain is divided into control volumes, as illustrated in Fig. 3.4.1. Each control volume, indexed by i, is a hollow sphere bounded by $r = r_{i-\frac{1}{2}}$ and $r = r_{i+\frac{1}{2}}$.

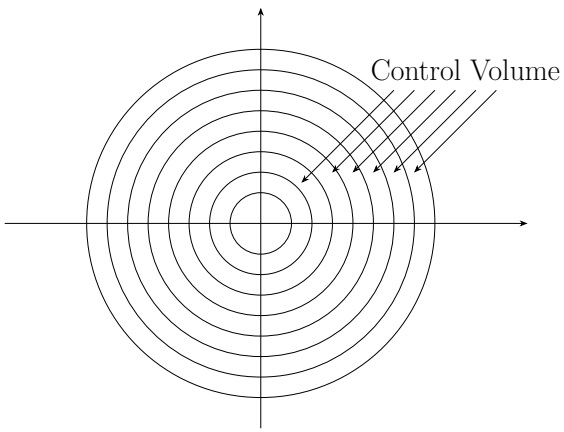

Figure 3: Spherical control volumes.

The governing equations of the model are:

$$\begin{cases} \frac{\partial \rho}{\partial t} + \frac{1}{r^2}\frac{\partial(\rho u r^2)}{\partial r} = 0; \\ \frac{\partial(\rho u)}{\partial t} + \frac{1}{r^2}\frac{\partial(\rho u^2 r^2)}{\partial r} = -\frac{\partial p}{\partial r}. \end{cases} \tag{12}$$

Integrating the continuity equation over the i-th control volume, whose volume is $V_i = \frac{(r^3_{i+\frac{1}{2}} - r^3_{i-\frac{1}{2}})}{3}$, yields:

$$\int_{V_i} \frac{\partial \rho}{\partial t}\, dV + \int_{V_i} \frac{1}{r^2}\frac{\partial(\rho u r^2)}{\partial r}\, dV = 0; \tag{13}$$

which can be written as:

$$\int_{r_{i-\frac{1}{2}}}^{r_{i+\frac{1}{2}}} \frac{\partial \rho}{\partial t} r^2 \, dr + \int_{r_{i-\frac{1}{2}}}^{r_{i+\frac{1}{2}}} \frac{1}{r^2} \frac{\partial (\rho u r^2)}{\partial r} r^2 \, dr = 0; \tag{14}$$

or equivalently:

$$\frac{d}{dt} \int_{r_{i-\frac{1}{2}}}^{r_{i+\frac{1}{2}}} \rho r^2 \, dr + \int_{r_{i-\frac{1}{2}}}^{r_{i+\frac{1}{2}}} \frac{1}{r^2} \frac{\partial (\rho u r^2)}{\partial r} r^2 \, dr = 0. \tag{15}$$

The cell-averaged density is defined as:

$$\rho_i = \frac{1}{V_i} \int_{V_i} \rho \, dV, \tag{16}$$

Hene, the continuity equation becomes:

$$\frac{d(\rho_i V_i)}{dt} + ((\rho u r^2)_{r_{i+\frac{1}{2}}} - (\rho u r^2)_{r_{i-\frac{1}{2}}}) = 0. \tag{17}$$

Integrating in time over a time step $\Delta t = t^{k+1} - t^k$ gives:

$$\int_{t^k}^{t^{k+1}} \frac{d(\rho_i V_i)}{dt} \, dt + \int_{t^k}^{t^{k+1}} ((\rho u r^2)_{r_{i+\frac{1}{2}}} - (\rho u r^2)_{r_{i-\frac{1}{2}}}) \, dt = 0. \tag{18}$$

The interface fluxes are defined as:

$$f^k_{r_{i\pm\frac{1}{2}}} = \frac{1}{\Delta t} \int_{t^k}^{t^{k+1}} (\rho u r^2)_{r_{i\pm\frac{1}{2}}} \, dt, \tag{19}$$

so that:

$$(\rho_i^{k+1} - \rho^k) V_i + \Delta t (f^k_{r_{i+\frac{1}{2}}} - f^k_{r_{i-\frac{1}{2}}}) = 0, \tag{20}$$

which leads to the discrete continuity equation:

$$\rho_i^{k+1} = \rho_i^k - \frac{\Delta t}{V_i} (f^k_{r_{i+\frac{1}{2}}} - f^k_{r_{i-\frac{1}{2}}}). \tag{21}$$

To discretize the momentum conservation equation, the pressure term must be treated appropriately. Consider:

$$\frac{\partial p}{\partial r} = \frac{r^2}{r^2} \frac{\partial p}{\partial r} = \frac{1}{r^2} \left(\frac{\partial (p r^2)}{\partial r} - p \frac{\partial r^2}{\partial r} \right) = \frac{1}{r^2} \left(\frac{\partial (p r^2)}{\partial r} - 2pr \right); \tag{22}$$

Substituting this into the momentum equation gives:

$$\frac{\partial (\rho u)}{\partial t} + \frac{1}{r^2} \frac{\partial ((\rho u^2 + p) r^2)}{\partial r} = \frac{2p}{r}. \tag{23}$$

Following the same procedure used for the continuity equation, the momentum balance equation becomes:

$$\int_{V_i} \frac{\partial (\rho u)}{\partial t} \, dV + \int_{V_i} \frac{1}{r^2} \frac{\partial ((\rho u^2 + p) r^2)}{\partial r} \, dV = \int_{V_i} \frac{2p}{r} \, dV, \tag{24}$$

that is equivalent to:

$$\int_{r_{i-\frac{1}{2}}}^{r_{i+\frac{1}{2}}} \frac{\partial(\rho u)}{\partial t} r^2\, dr + \int_{r_{i-\frac{1}{2}}}^{r_{i+\frac{1}{2}}} \frac{1}{r^2} \frac{\partial((\rho u^2 + p) r^2)}{\partial r} r^2\, dr = \int_{r_{i-\frac{1}{2}}}^{r_{i+\frac{1}{2}}} \frac{2p}{r} r^2\, dr. \tag{25}$$

The pressure source term can be rewritten as:

$$\int_{r_{i-\frac{1}{2}}}^{r_{i+\frac{1}{2}}} 2pr\, dr = ((pr^2)_{r_{i+\frac{1}{2}}} - (pr^2)_{r_{i-\frac{1}{2}}}) - \int_{r_{i-\frac{1}{2}}}^{r_{i+\frac{1}{2}}} \frac{\partial p}{\partial r} r^2\, dr. \tag{26}$$

The cell-averaged radial pressure gradient is defined as:

$$\left(\frac{\partial p}{\partial r}\right)_i = \frac{1}{V_i} \int_{r_{i-\frac{1}{2}}}^{r_{i+\frac{1}{2}}} \frac{\partial p}{\partial r} r^2\, dr. \tag{27}$$

and thus:

$$\int_{r_{i-\frac{1}{2}}}^{r_{i+\frac{1}{2}}} 2pr\, dr = ((pr^2)_{r_{i+\frac{1}{2}}} - (pr^2)_{r_{i-\frac{1}{2}}}) - \left(\frac{\partial p}{\partial r}\right)_i V_i. \tag{28}$$

The integrated momentum equation is therefore:

$$\frac{d}{dt} \int_{r_{i-\frac{1}{2}}}^{r_{i+\frac{1}{2}}} \rho u r^2\, dr + \int_{r_{i-\frac{1}{2}}}^{r_{i+\frac{1}{2}}} \frac{1}{r^2} \frac{\partial((\rho u^2 + p) r^2)}{\partial r} r^2\, dr = ((pr^2)_{r_{i+\frac{1}{2}}} - (pr^2)_{r_{i-\frac{1}{2}}}) - \left(\frac{\partial p}{\partial r}\right)_i V_i. \tag{29}$$

Proceeding analogously to the mass conservation equation gives:

$$(\rho u)_i^{k+1} = (\rho u)_i^k - \frac{\Delta t}{V_i}(f^k_{r_{i+\frac{1}{2}}} - f^k_{r_{i-\frac{1}{2}}}) + \frac{\Delta t}{V_i}(((pr^2)^k_{r_{i+\frac{1}{2}}} - (pr^2)^k_{r_{i-\frac{1}{2}}}) - \Delta t \left(\frac{\partial p}{\partial r}\right)_i^k \tag{30}$$

where

$$f^k_{r_{i\pm\frac{1}{2}}} = \frac{1}{\Delta t} \int_{t^k}^{t^{k+1}} ((\rho u^2 + p) r^2)_{r_{i\pm\frac{1}{2}}}\, dt. \tag{31}$$

$$(pr^2)^k_{r_{i\pm\frac{1}{2}}} = \frac{1}{\Delta t} \int_{t^k}^{t^{k+1}} (pr^2)_{r_{i\pm\frac{1}{2}}}\, dt. \tag{32}$$

$$\left(\frac{\partial p}{\partial r}\right)_i^k = \frac{1}{\Delta t} \int_{t^k}^{t^{k+1}} \left(\frac{\partial p}{\partial r}\right)_i dt. \tag{33}$$

The i-th cell pressure gradient can be expressed as:

$$\left(\frac{\partial p}{\partial r}\right)_i^k = \frac{p^k_{r_{i+\frac{1}{2}}} - p^k_{r_{i-\frac{1}{2}}}}{\Delta r}, \tag{34}$$

where $\Delta r = r_{i+\frac{1}{2}} - r_{i-\frac{1}{2}}$ and $p^k_{r_{i\pm\frac{1}{2}}}$ is the pressure evaluated at time step k and $r = r_{i\pm\frac{1}{2}}$.

The discretized momentum equation is then:

$$(\rho u)_i^{k+1} = (\rho u)_i^k - \frac{\Delta t}{V_i}(f^k_{r_{i+\frac{1}{2}}} - f^k_{r_{i-\frac{1}{2}}}) + \frac{\Delta t}{V_i}(((pr^2)^k_{r_{i+\frac{1}{2}}} - (pr^2)^k_{r_{i-\frac{1}{2}}}) - \frac{\Delta t}{\Delta r}(p^k_{r_{i+\frac{1}{2}}} - p^k_{r_{i-\frac{1}{2}}}). \tag{35}$$

The discrete system to be implemented is:

$$\begin{cases} \rho_i^{k+1} = \rho_i^k - \frac{\Delta t}{V_i}(f^k_{r_{i+\frac{1}{2}}} - f^k_{r_{i-\frac{1}{2}}}), \\ (\rho u)_i^{k+1} = (\rho u)_i^k - \frac{\Delta t}{V_i}(f^k_{r_{i+\frac{1}{2}}} - f^k_{r_{i-\frac{1}{2}}}) + \frac{\Delta t}{V_i}(((pr^2)^k_{r_{i+\frac{1}{2}}} - (pr^2)^k_{r_{i-\frac{1}{2}}}) - \frac{\Delta t}{\Delta r}(p^k_{r_{i+\frac{1}{2}}} - p^k_{r_{i-\frac{1}{2}}}). \end{cases} \tag{36}$$

To solve the discrete system, the interface numerical fluxes must first be determined; once available, time integrations can be performed.

3.4.2 Riemann Problem

Consider a governing equation system such as the model one:

$$\begin{cases} \frac{\partial \rho}{\partial t} + \frac{1}{r^2}\frac{\partial(\rho u r^2)}{\partial r} = 0; \\ \frac{\partial(\rho u)}{\partial t} + \frac{1}{r^2}\frac{\partial(\rho u^2 r^2)}{\partial r} = -\frac{\partial p}{\partial r}. \end{cases} \tag{37}$$

the system first equation can be rewritten as:

$$\frac{\partial(\rho r^2)}{\partial t} + \frac{\partial(\rho u r^2)}{\partial r} = 0, \tag{38}$$

and thus the second one can be written as:

$$u\left[\frac{\partial(\rho r^2)}{\partial t} + \frac{\partial(\rho u r^2)}{\partial r}\right] + \rho r^2 \frac{\partial u}{\partial t} + \rho u r^2 \frac{\partial u}{\partial r} = -r^2 \frac{\partial p}{\partial r}, \tag{39}$$

that leads, taking into account the continuity equation, to:

$$\rho r^2 \frac{\partial u}{\partial t} + \rho u r^2 \frac{\partial u}{\partial r} = -r^2 \frac{\partial p}{\partial r}. \tag{40}$$

Dividing by ρr^2, it is possible to write:

$$\frac{\partial u}{\partial t} + u\frac{\partial u}{\partial r} = -\frac{1}{\rho}\frac{\partial p}{\partial r}; \tag{41}$$

it is possible to note that:

$$\frac{\partial p}{\partial r} = \frac{\partial p}{\partial \rho r^2}\frac{\partial \rho r^2}{\partial r} = \frac{\partial p}{\partial \rho}\frac{\partial \rho}{\partial \rho r^2}\frac{\partial \rho r^2}{\partial r} = \frac{\partial p}{\partial \rho}\left(\frac{\partial \rho r^2}{\partial \rho}\right)^{-1}\frac{\partial \rho r^2}{\partial r} = \frac{1}{r^2}\frac{\partial p}{\partial \rho}\frac{\partial \rho r^2}{\partial r}. \tag{42}$$

So the second equation of the governing system can be write as:

$$\frac{\partial u}{\partial t} + u\frac{\partial u}{\partial r} + \frac{1}{\rho r^2}\frac{\partial p}{\partial \rho}\frac{\partial \rho r^2}{\partial r} = 0. \tag{43}$$

The governing system is thus expressed in linear form as below:

$$\begin{pmatrix} \rho r^2 \\ u \end{pmatrix}_t + \begin{pmatrix} u & \rho r^2 \\ \frac{c^2}{\rho r^2} & u \end{pmatrix} \begin{pmatrix} \rho r^2 \\ u \end{pmatrix}_r = 0.$$

From now on, the variable vector will be denoted as $\mathbf{q}$ and the coefficient matrix as $\mathbf{A}$ It is possible to decouple the equation by diagonalizing A.
In order to do this, eigenvalues and eigenvectors of the matrix need to be calculated:

$$det \begin{pmatrix} u-\lambda & \rho r^2 \\ \frac{c^2}{\rho r^2} & u-\lambda \end{pmatrix} = 0$$

leading to:

$$\lambda_1 = u - c \qquad \lambda_2 = u + c. \tag{44}$$

The eigenvectors associated with those eigenvalues are the following ones:

$$\mathbf{e_1} = \begin{pmatrix} 1 \\ -\frac{c}{\rho r^2} \end{pmatrix} \qquad \mathbf{e_2} = \begin{pmatrix} 1 \\ \frac{c}{\rho r^2} \end{pmatrix}.$$

Let $\mathbf{R}$ be the eigenvectors matrix, defined as:

$$R = \begin{pmatrix} 1 & 1 \\ -\frac{c}{\rho r^2} & \frac{c}{\rho r^2}. \end{pmatrix}$$

It it possible to write:

$$\mathbf{R^{-1}q_t + R^{-1}ARR^{-1}q_r = 0} \tag{45}$$

and thus to obtain a decoupled system, as $R^{-1}AR$ is a diagonal matrix. In particular:

$$\mathbf{R^{-1}dq} = \begin{pmatrix} \frac{1}{2} & \frac{-\rho r^2}{2c} \\ \frac{1}{2} & \frac{\rho r^2}{2c} \end{pmatrix} \begin{pmatrix} d\rho r^2 \\ du \end{pmatrix} = \begin{pmatrix} \frac{d\rho r^2}{2} - \left(\frac{\rho r^2}{2c}\right) du \\ \frac{d\rho r^2}{2} + \left(\frac{\rho r^2}{2c}\right) du \end{pmatrix}$$

In the end, the system can be write as:

$$\begin{pmatrix} \frac{\rho r^2}{2} - \left(\frac{\rho r^2}{2c}\right) u \\ \frac{\rho r^2}{2} + \left(\frac{\rho r^2}{2c}\right) u \end{pmatrix}_t + \begin{pmatrix} u-c & 0 \\ 0 & u+c \end{pmatrix} \begin{pmatrix} \frac{\rho r^2}{2} - \left(\frac{\rho r^2}{2c}\right) u \\ \frac{\rho r^2}{2} + \left(\frac{\rho r^2}{2c}\right) u \end{pmatrix}_r = 0.$$

This system express the conservations of certain quantites along specific lines in the space-time phase plane.
In particular, the conservation quantities, known as Riemann Invariants, are:

$$\mathbf{w} = \begin{pmatrix} \frac{\rho r^2}{2} - \left(\frac{\rho r^2}{2c}\right) u \\ \frac{\rho r^2}{2} + \left(\frac{\rho r^2}{2c}\right) u \end{pmatrix}$$

and they are, respectively conserved along so called characteristics lines which are identified by their slopes. In the analyzed problem, the calculates characteristic slopes are:

$$\begin{pmatrix} u-c \\ u+c \end{pmatrix}.$$

In the end, the governing equation system can be expressed as:

$$dw_1 = \frac{d\rho r^2}{2} - \left(\frac{\rho r^2}{2c}\right) du = 0 \tag{46}$$

along a characteristic line identified by slope $u - c$, while

$$dw_2 = \frac{d\rho r^2}{2} + \left(\frac{\rho r^2}{2c}\right) du = 0 \tag{47}$$

along a characteristic line identified by slope $u + c$.
It is possible to simplify the $dw_{1,2}$ expressions as follow:

$$dw_{1,2} = \frac{d\rho r^2}{\rho r^2} \pm \left(\frac{1}{c}\right) du = 0 \tag{48}$$

$$dw_{1,2} = \frac{d\rho r^2}{c\rho r^2} \pm \left(\frac{1}{c^2}\right) du = 0 \tag{49}$$

$$dw_{1,2} = \frac{d\rho r^2}{c\rho r^2} \pm \left(\frac{1}{\frac{\partial p}{\partial \rho}}\right) du = 0 \tag{50}$$

$$dw_{1,2} = \frac{d\rho r^2}{c\rho r^2} \pm \left(\frac{1}{\frac{\partial p}{\partial \rho r^2}\frac{\partial \rho r^2}{\partial \rho}}\right) du = 0 \tag{51}$$

$$dw_{1,2} = \frac{d\rho r^2}{c\rho r^2} \pm \left(\frac{1}{r^2\frac{\partial p}{\partial \rho r^2}}\right) du = 0 \tag{52}$$

$$dw_{1,2} = \frac{dp}{c\rho} \pm du = 0 \tag{53}$$

$$dw_{1,2} = dp \pm (c\rho) du = 0 \tag{54}$$

Consider now a reconstruction interface discontinutity such as the one reported in Fig. 4.
This disconinuity outcomes need to be investigated to adress the interface fluxes in the discretized problem previously introuduced.
This problem is referred to as the Riemann problem.

On the space-time phase plane, the discontinuty allows the propagation of two kind of signals along the previosly introduced characteristics lines, as shown in Fig. 5.
Since velocity and sound speed are not constant, the characteristic slopes are space-dependent. Therefore, the characteristics are divided into two families, each one identified by its own slope expression.

As shown in figure 5, an intermediate zone, called *Zone c* develops between the two cell states, named *Zone a* and *Zone b*.

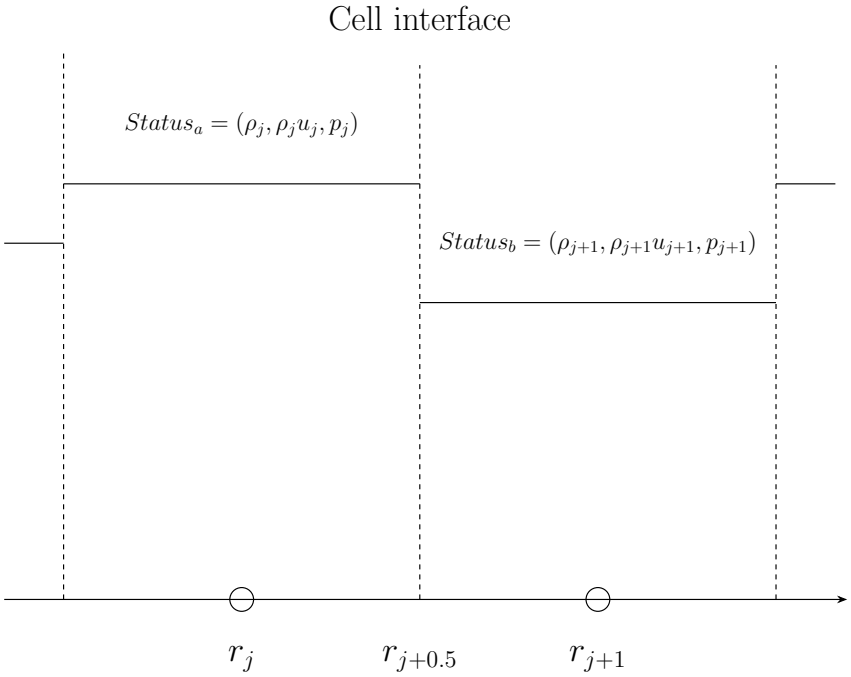

Figure 4: Initial Riemann problem situation.

The first family of characteristics has slopes in the range $[u_a - c_a, u_c - c_c]$ range, while the second family has slopes in the range $[u_c + c_c, u_b + c_b]$.

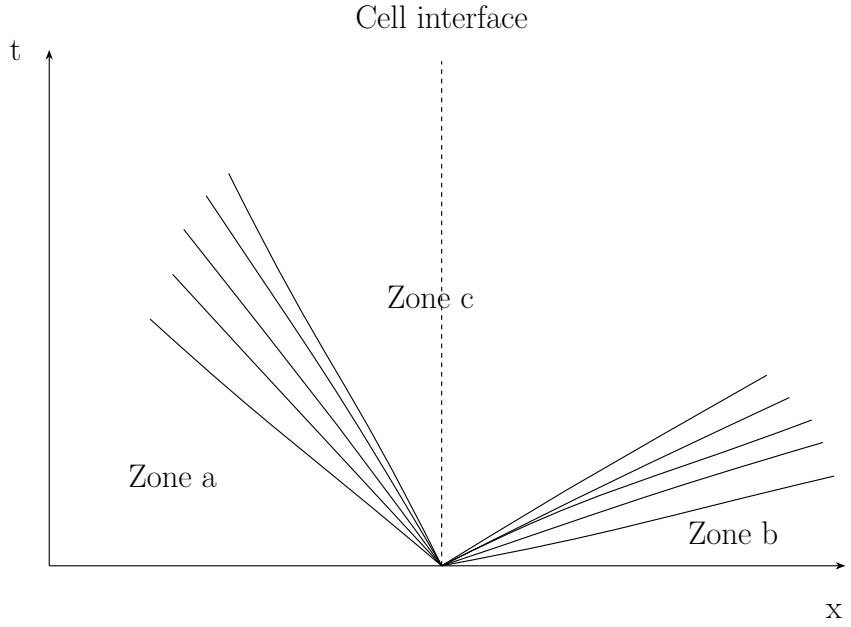

Figure 5: Example of discontinuity outcomes.

The simple-wave hypothesis is taken into account, meaning that only one wave from one of the characteristic families can be considered in isolation. Under this assumption, it is possible to identify $Zone\, c$ using the conservation of the Riemann invariants along the characteristic lines, as follows:

- **First family characteristics rarefaction of compression**

  For the first family of characteristics, the expansion or compression from $Zone\,a$ to $Zone\,c$ is characterised by $dw_2 = 0$, thus, considering the equation as linearized, it is possible to write:

$$dp + (\rho c)_a du = 0 \tag{55}$$

$$p_a + (\rho c)_a u_a = p_c + (\rho c)_a u_c \tag{56}$$

- **Second family characteristics rarefaction of compression**

  For the second family of characteristics, the expansion or compression from $Zone\,c$ to $Zone\,b$ is characterised by $dw_1 = 0$, thus, considering the equation as linearized, it is possible to write:

$$dp - (\rho c)_b du = 0 \tag{57}$$

$$p_b - (\rho c)_b u_b = p_c - (\rho c)_b u_c \tag{58}$$

- **Zone c status definition**

  Combining the equations for first and second rarefactions or compressions, it is pobbile to write the following system:

$$\begin{cases} p_a + (\rho c)_a u_a = p_c + (\rho c)_a u_c \\ p_b - (\rho c)_b u_b = p_c - (\rho c)_b u_c \end{cases} \tag{59}$$

  Once solved, considering the closure law $\rho(p)$, u_c and p_c define the whole $Zone\,c$; all the needed information to solve the Riemann Problem are then available.

Signals propagation direction

Depending on the flow properties, the characteristics slopes can be positive or negative. Should the characteristic slopes be negative, the signals are reported as being left-forwarded. Conversely, if the characteristic slopes are positive, the signals are reported as being right-forwarded. Furthermore, these signs are indicative of the solution to the Riemann problem. The possible recostruction discontinuities outcomes are reported below.

- Both characteristic families expansions 6 ;

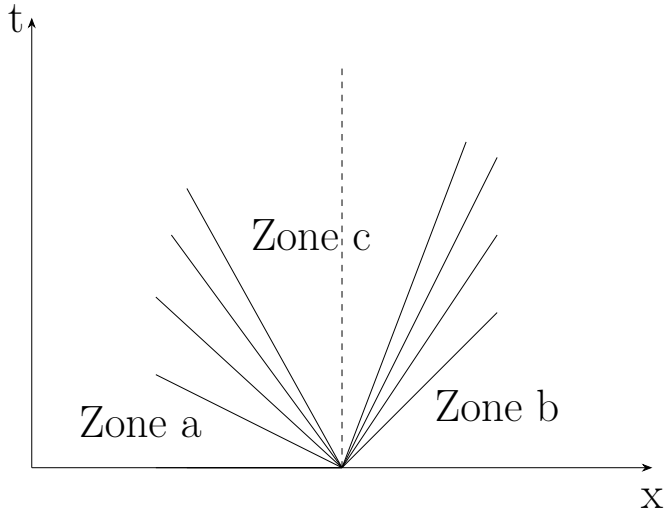

Figure 6: Expansions of first and second families.

- First characteristics family compression and second characteristics family expansion 7;

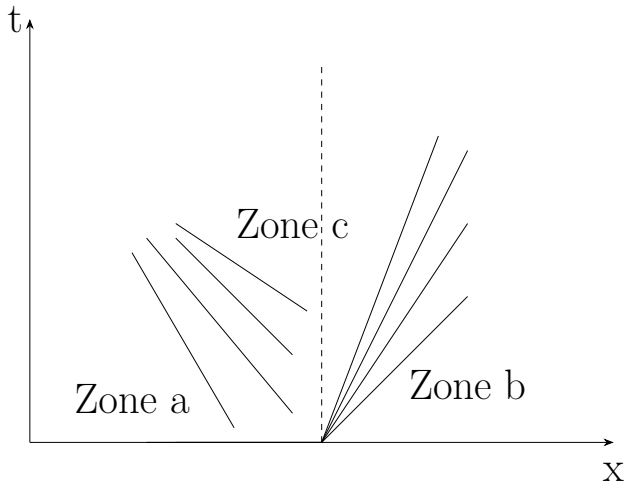

Figure 7: Compression of first family and expansion of the second one.

- Both families compression 8;

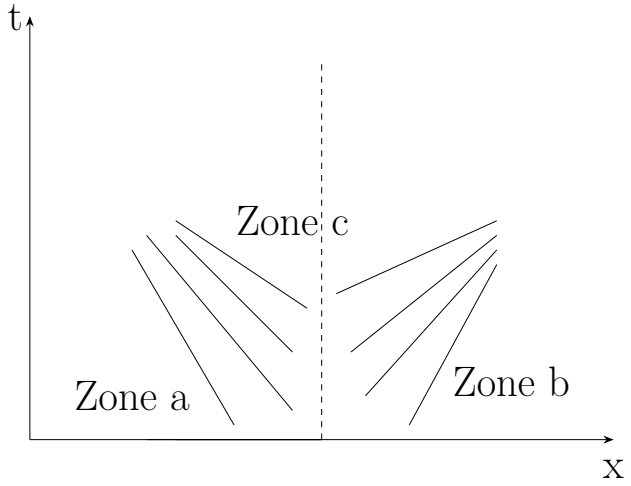

Figure 8: Both families compression.

- Expansion of the first family and compression of the second one 9;

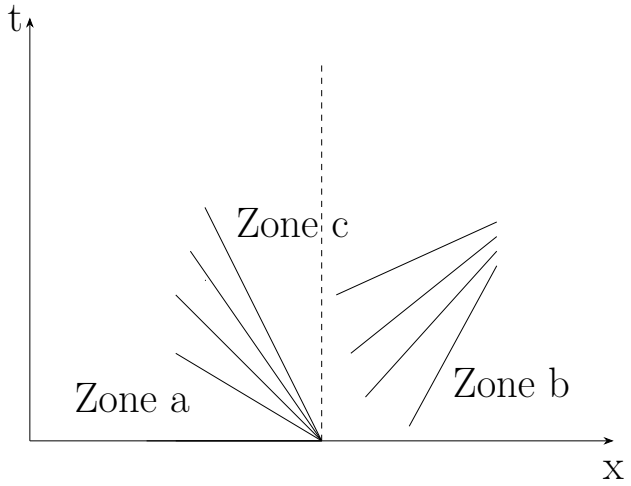

Figure 9: Expansion of the first family and compression of the second one.

- Transonic expansion of first family and expansion of the second one 10;

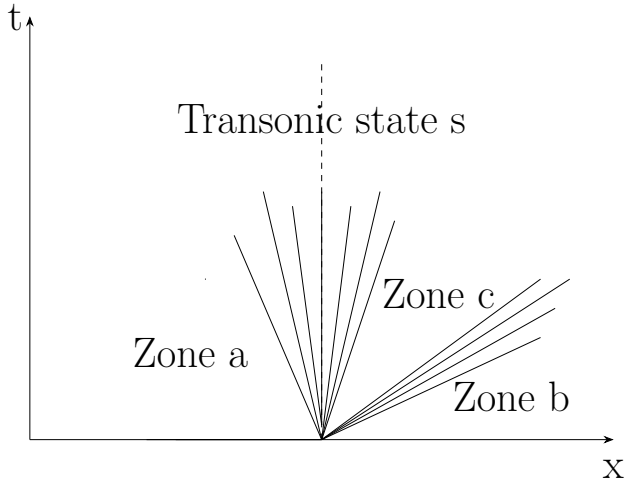

Figure 10: Transonic expansion of first family and expansion of second family.

- Transonic expansion of first family and compression of the second one 11;

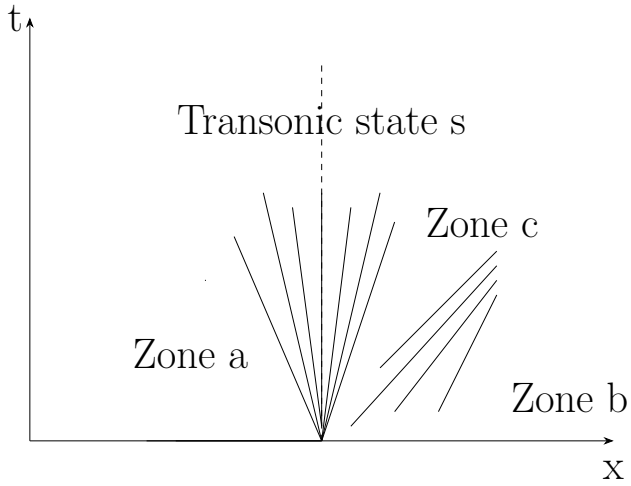

Figure 11: Transonic expansion of first family and compression of second family.

- Expansion of the first family and transonic expansion of the second one 12;

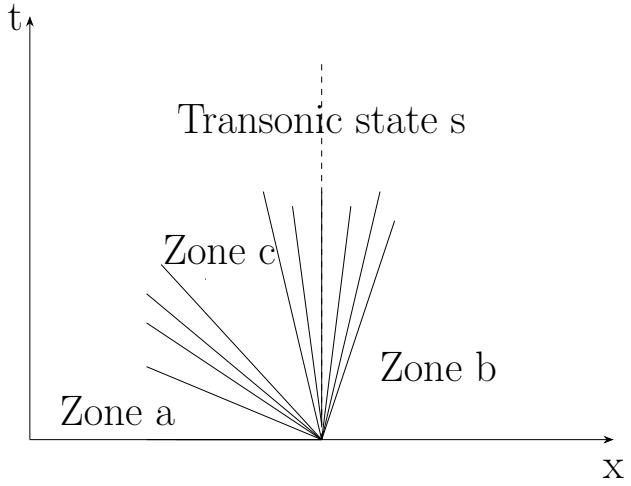

Figure 12: Expansion of the first family and transonic expansion of the second one.

- Compression of the first family and transonic expansion of the second one 13;

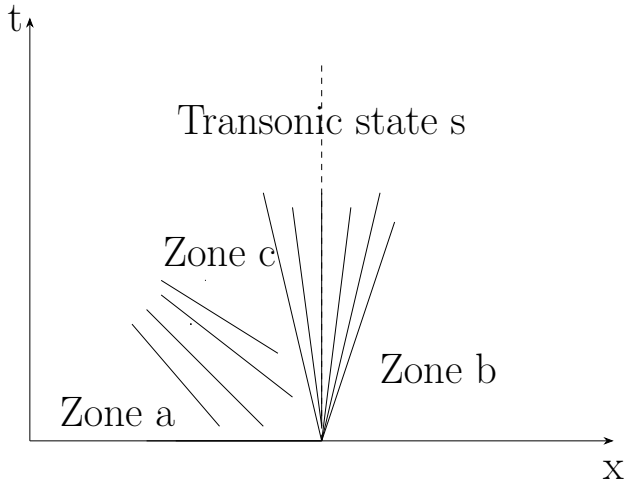

Figure 13: Compression of the first family and transonic expansion of the second one.

- Compression of first family and transonic compression of the second one 14;

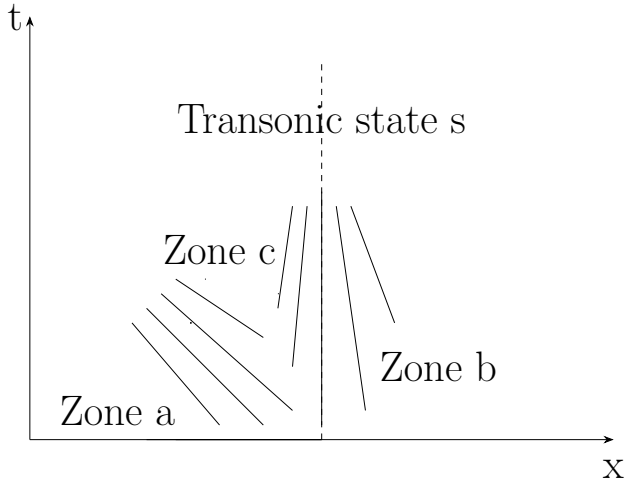

Figure 14: Compression of first family and transonic compression of the second one.

- Expansion of first family and transonic compression of the second one 15;

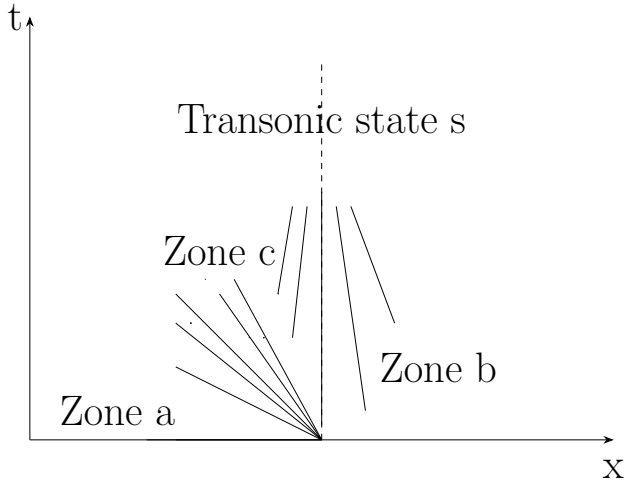

Figure 15: Expansion of first family and transonic compression of the second one.

- Transonic compression of first family and expansion of the second one 16;

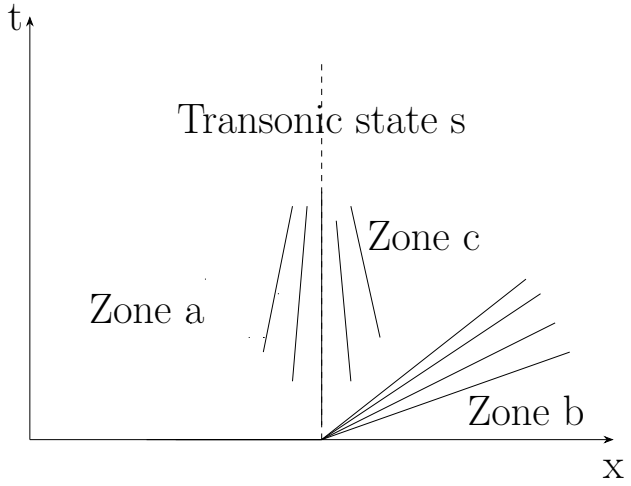

Figure 16: Transonic compression of first family and expansion of the second one.

- Transonic compression of first family and compression of the second one 17.

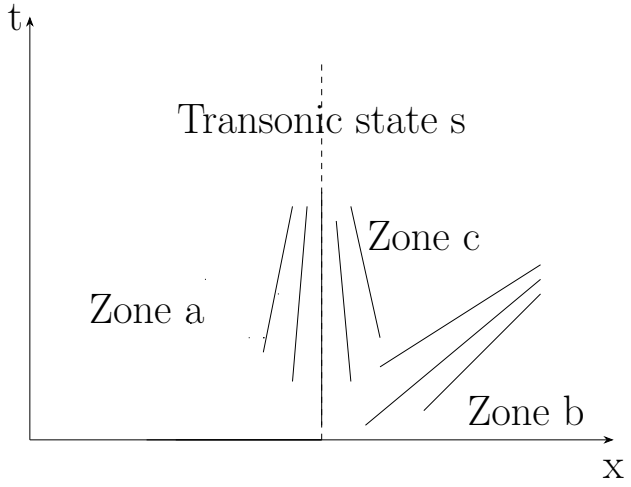

Figure 17: Transonic compression of first family and compression of the second one.

From a physical point of view, a compression of a family of characteristics results in a shock, which velocity can be described using the Rankine Hugoiont jump conditions [14].
Each above reported possibility define an interface status needed to calculate the numeirical interface fluxes.
A **Riemann Solver** is thus required to recognize the discontinuity outcomes (i.e. identify which of the above outcomes has been produced at ech cells interfae) and then calculate the interface fluxes.

An **exact Riemann Solver** operates trough the following algorithm:

- Evaluate the status a and b of the interface neighboring cells;
- Use the Riemnann Invariants to identify the $Zone\, c$;
- Determine which one of the above discontinuity outcomes occurs at the interface;
- Compute the eventually shock velocity as explained in [14];
- Eventually calculate the transonic status (using the Riemann Invariants as mentioned for the $Zone\, c$ calculation taking into account the transonic condition);
- Use the characteristics slopes signs and the expansion/shock conditions to figure out the interface fluxes (this process is presented in the following section);

To reduce the computation costs of an exact Riemann solver, approximate solvers have been introduced. The implemented solver of this work is an **Osher solver**, which differs from an exact solver by approximating shocks as a compressions families. In this way, the algorithm is reduced to:

- Evaluate the status a and b of the interface neighboring cells;
- Use the Riemann Invariants to identify $Zone\, c$;
- Determine which one of the above discontinuity outcomes occurs at the interface;
- Eventually calculate the transonic status (using the Riemann Invariants as mentioned for the $Zone\, c$ calculation taking into account the transonic condition);
- Use the characteristics slopes signs to figure out the interface fluxes (this process is presented in the following section);

This algorithm is applied to each cell interface and the interface fluxes are thus available to perform time integrations.

3.4.3 Interface fluxes

Consider to investigate the interface $i - \frac{1}{2}$. Then, the following quantities can be derived:

$$\begin{cases} \overrightarrow{\Delta f}_{i-\frac{1}{2}} = \frac{1-\sigma_1}{2}(f_c - f_a) + \frac{1-\sigma_2}{2}(f_b - f_c) \\ \overleftarrow{\Delta f}_{i-\frac{1}{2}} = \frac{1+\sigma_1}{2}(f_c - f_a) + \frac{1+\sigma_2}{2}(f_b - f_c) \end{cases} \tag{60}$$

where

$$\sigma_i = \begin{cases} +1 & if\, ith\, signal\, is\, right - forwarded \\ -1 & otherwise \end{cases} \tag{61}$$

In the transonic case, the introduced $\Delta f_{i-\frac{1}{2}}$ are:

- First family transonic expansion:

$$\begin{cases} \overrightarrow{\Delta f}_{i-\frac{1}{2}} = f_b - f_s \\ \overleftarrow{\Delta f}_{i-\frac{1}{2}} = f_s - f_a \end{cases} \tag{62}$$

- First family transonic compression:

$$\begin{cases} \overrightarrow{\Delta f}_{i-\frac{1}{2}} = (f_s - f_a) + (f_b - f_c) \\ \overleftarrow{\Delta f}_{i-\frac{1}{2}} = f_c - f_s \end{cases} \tag{63}$$

- Second family transonic expansion:

$$\begin{cases} \overrightarrow{\Delta f}_{i-\frac{1}{2}} = f_b - f_s \\ \overleftarrow{\Delta f}_{i-\frac{1}{2}} = f_s - f_a \end{cases} \tag{64}$$

- Second family transonic compression:

$$\begin{cases} \overrightarrow{\Delta f}_{i-\frac{1}{2}} = f_s - f_c \\ \overleftarrow{\Delta f}_{i-\frac{1}{2}} = (f_c - f_a) + (f_b - f_s) \end{cases} \tag{65}$$

The interface fluxes are calculated as:

$$f^k_{i-\frac{1}{2}} = f(u_i) - \overrightarrow{\Delta f}_{i-\frac{1}{2}} \tag{66}$$

but also as:

$$f^k_{i-\frac{1}{2}} = f(u_{i-1}) + \overleftarrow{\Delta f}_{i-\frac{1}{2}} \tag{67}$$

Thus, different outcomes produce the following results:

- Transonic expansion of one of the two families of characteristics: $f^k_{i-\frac{1}{2}} = f(u_s)$;
- Transonic compression of first family : $f^k_{i-\frac{1}{2}} = f(u_a) + f(u_c) - f(u_s)$;
- Transonic compression of second family : $f^k_{i-\frac{1}{2}} = f(u_b) + f(u_c) - f(u_s)$;
- Any other case : $f^k_{i-\frac{1}{2}} = f(u_c)$.

Following this approach, the Osher solver can perform the numerical integration through the above described algorithm.

3.4.4 Multifluid interface treatment- Ghost Fluid Method

The compressible multifluid interface is treated using the ghost fluid method proposed in [11]. The aim of the method is to perform the time integration in many one-media sub-domain instead of doing it on one multimedia domain. In order to do that, the domain is at first divided into two zone, respectively the water one and the lead one as shown in Fig. 18

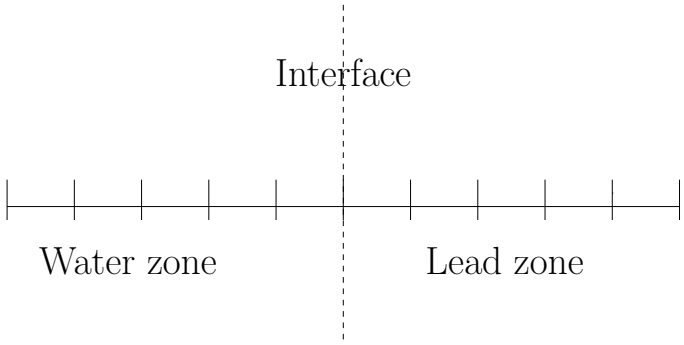

Figure 18: Expamle of divided domain.

Once divided, some cells, named ghost cells, are added to water and lead domains 19. The number of cells to be added depends on the reconstruction order. Ghost cells are considered as an extension of one fluid into another's domain, therefore, their properties are the same as those of the fluid they are extending.

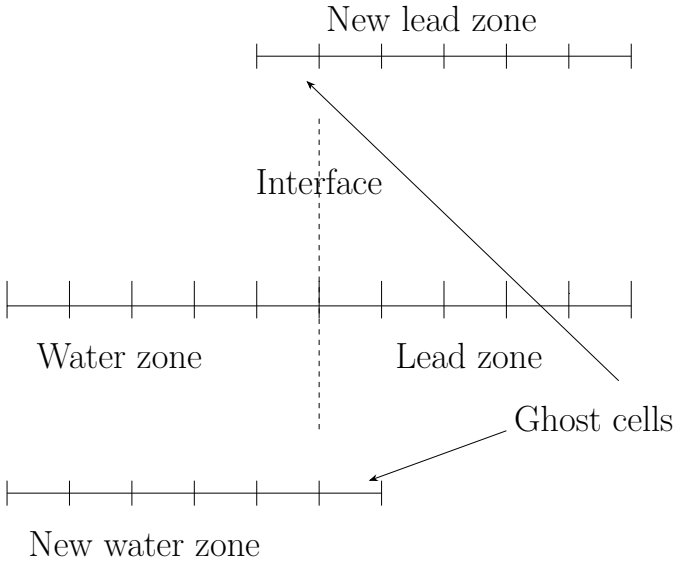

Figure 19: New domains taking into account water cells. Example for a first order recostruction.

The method involves two interactions:

- A **real interaction** between the two fluids.
- A **ghost interaction** for each fluid.

Real interaction

Supposing an interaction between the last real water cell and the first real lead cell. As expalined above, an intermediate zone ($Zone\, c$) develops across discontinuities in physical quantities (not only numerical ones). Riemann invariants are thus used to calculate pressure and velocity in this intermediate status:

$$\begin{cases} u_I = u_w - \int_{p_w}^{p_I} \frac{dp}{\rho_w c_w} \\ u_I = u_l + \int_{p_l}^{p_I} \frac{dp}{\rho_l c_l} \end{cases} \tag{68}$$

Ghost interaction

A ghost interaction occurs when a real cell of one fluid interacts with its ghost cell. The aim is to achieve the same interface conditions as for real interaction at each ghost interface (Fig. 20). In other words, the produced pressure and velocity at the ghost interfaces should be the same as at the real water-lead interface (p_I, u_I).

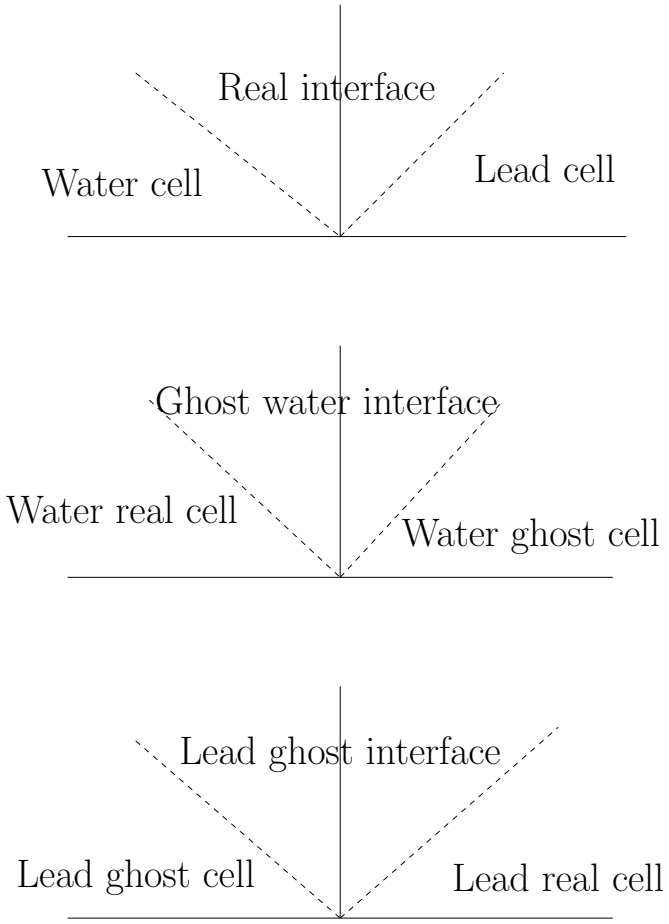

Figure 20: Real and ghost interfaces.

In order to correctly solve the multimedia interface, it is thus required a valuable initialization of the ghost cell for each fluid.

As proposed in [11], to obtain the real interface conditions on the ghost interfaces, it is possible to initialize the ghost cells status as the real interface ones, so:

$$Ghost\,cell\,state = (p_I, u_I, \rho(p_I)) \tag{69}$$

where the $\rho(p_I)$ closure laws depends by the fluid that the ghost cell is expanding (i.e., the water ghost cell behaves following the water closure law as the lead ghost cell behaves following the lead closure law). Once initialized the ghost cells, a time integration can be performed over two distinct domains (water and lead ones). The implemented alghoritm is then:

- Identify the water-lead interface;
- Divide the domain;
- Initializing ghost cells for each fluid;
- Perform a time integration over two distinct domain to update the real cells following the above described algorithm;
- Use the updated flowfield to calculate the new water-lead interface position

To track the interface a level set was implemented as proposed in [11]. Once a signed distance function ϕ such that $|\nabla\phi| = 1$ has been defined (negative in the water domain, zero on the interface and positive elsewhere), its update follows this equation:

$$\phi_t + u_I\phi_r = 0 \tag{70}$$

where u_I is the interface velocity above introduced.

The zero level-set position is approximated to the nearest cell interface. When the interface pass trough a cell and the water domain changes, the flow filed is updated by substituting the late lead cell flow field with the last calculated flow filed of water ghost cell as proposed in [15].

3.5 Numerical results and grid convergence

The above approches were implemented to solve the SIM governing equations. To evaluate the mesh impact, a grid convergence study was also performed and its results are provided in the folowing sections.

3.5.1 Code structure

The model was implemented in Python using an object-oriented approach and consists of six classes, as follows:

- Input class: Reads an external YAML file, setted by the user, in order to intialize the needed simulation data.
- Material class: Provides all the materials physical equations.
- Riemann Solver class: Performs time integrations and updates the flow field.
- Level set class: Manages the water-lead interface as above described.
- Results class : Stores the simulation results and save them in a dedicated file.
- Post Processing class: Provides useful tools to perform calculations post processing.

3.5.2 Calculation outcomes

The calculations were performed for a time range of $[0.0, 0.00021]\,s$, as the simulations matter of interest was limited to the initial flow filed behaviour. A CFL value of 0.6 was set. The considered mesh is a 10000 uniform elements mesh. A first order recostruction was produced.
The initial conditions were the following ones:

- $p_{w,0} = 18.0\,MPa$
- $p_{l,0} = 0.8\,MPa$
- $R_{w,0} = 0.013\,m$

The obtained radial pressure and velocity distributions at different times are reported in 21 and 22.

As can be seen, the shock front propagates rapidly through the lead pool (at approximately the speed of sound in lead), but its value also decreases rapidly. Additionally, radial velocity increases from the material interface throughout the radial domain. It is also notable that the flow field develops quickly, which is why the simulations were limited to a short time range.
These information are useful to evauluate the consequences of the SGTR accident scenario on the reactor mechanical parts, in particular the impact of the shock wave on the others steam generator tubes. To investigate this data, the pressure time evolution at multiple radius is useful, and its reported in Fig. 23.
It is notable that once the shock wave reaches a certain radial coordinate, the pressure tends to remain constant at that value.

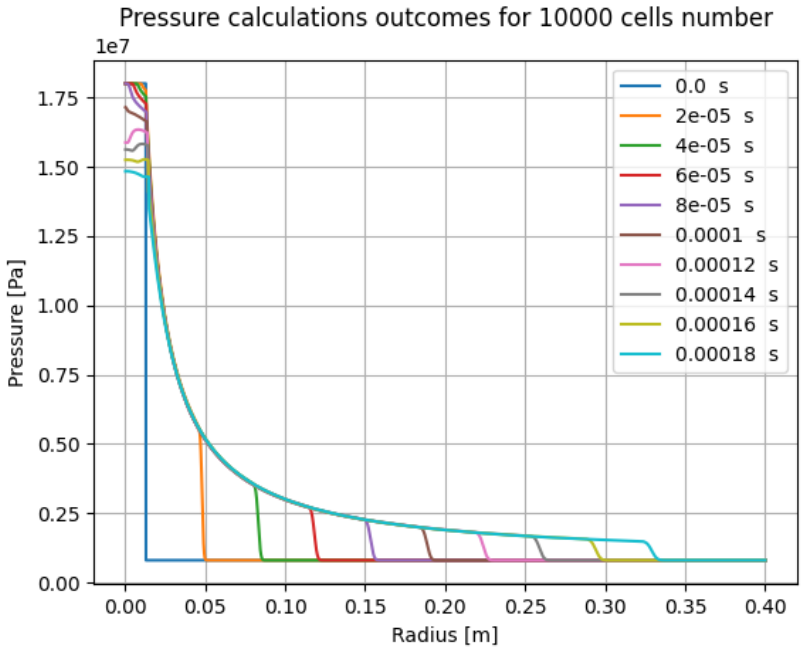

Figure 21: Calculations outcomes: radial pressure at multiples times for 10000 elements mesh.

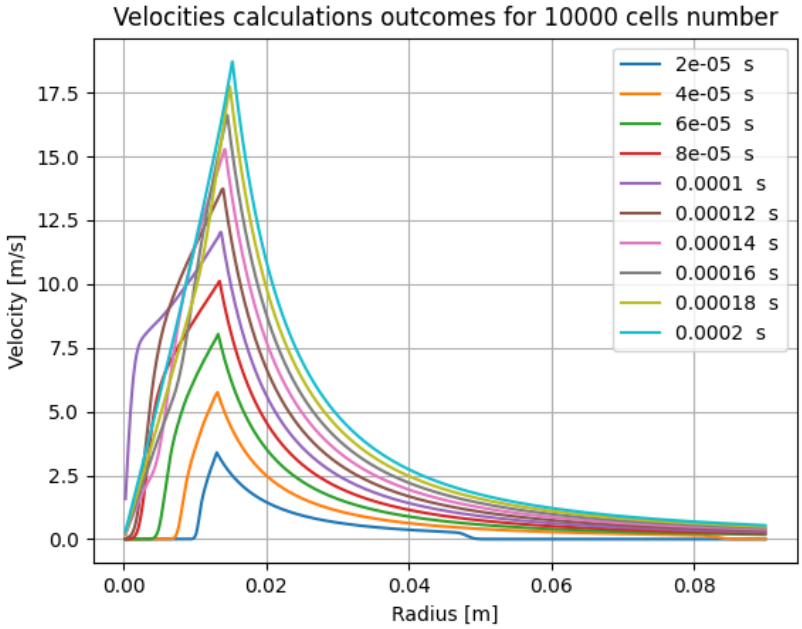

Figure 22: Calculations outcomes: radial velocity at multiples times for 10000 elements mesh.

3.5.3 Comparison with reference data

Comparisons with reference data are reported below.
The reference data are obtained with an high-order recostruction and in a uniform 1000 elements mesh. It can be seen that, due to the low order of recostruction, the calculations outcomes are affected by numerical diffusion: this phenomenon is easly

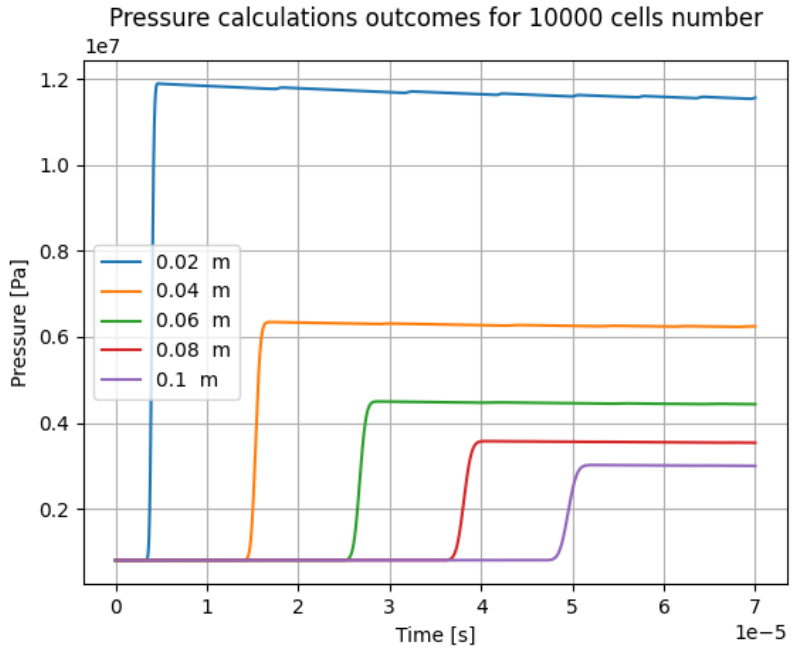

Figure 23: Calculations outcomes: pressure time evolution for 10000 elements mesh.

visible in Fig. 35 as the pressure at $0.02\,m$ should remain constant but it doesn't.

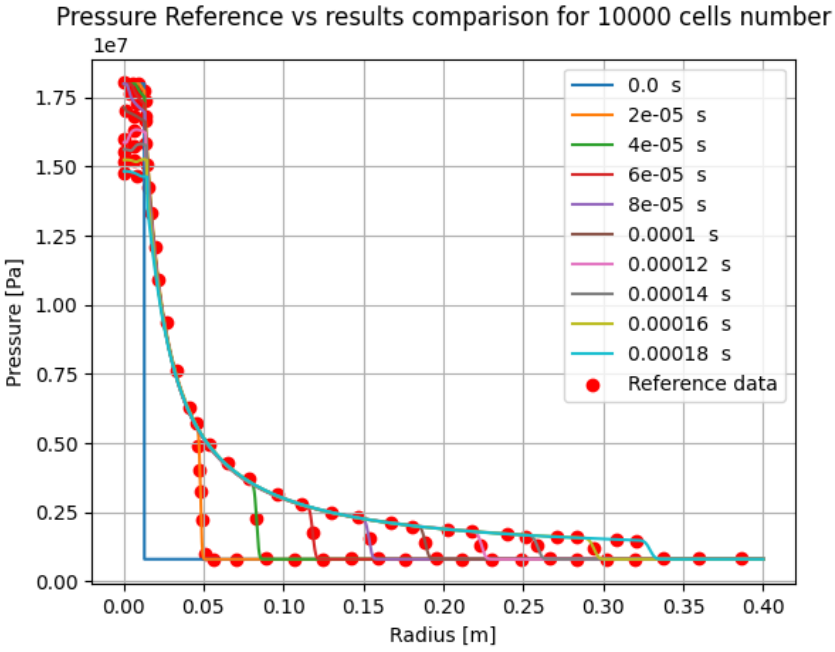

Figure 24: Radial pressure distribution at multiple times: comparison between present results and reference solution (10,000-element mesh).

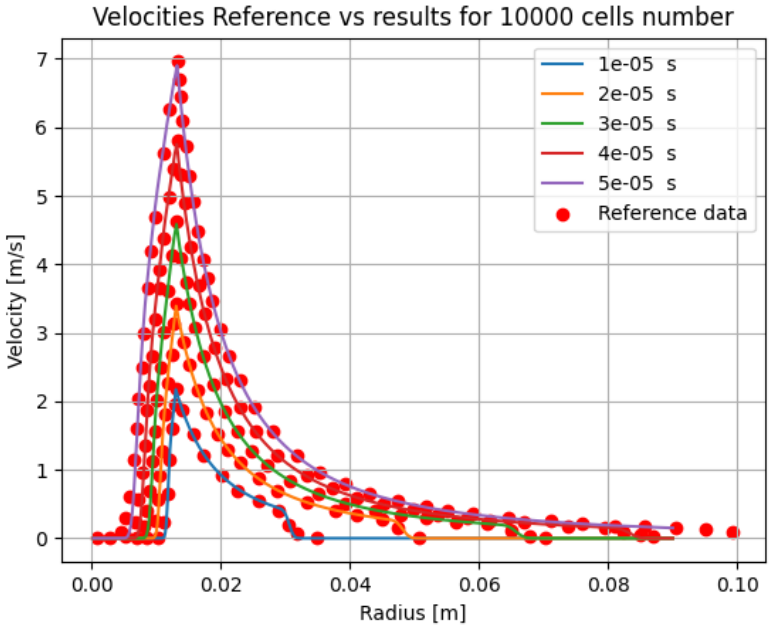

Figure 25: Radial velocity distribution at multiple times: comparison between present results and reference solution (10,000-element mesh).

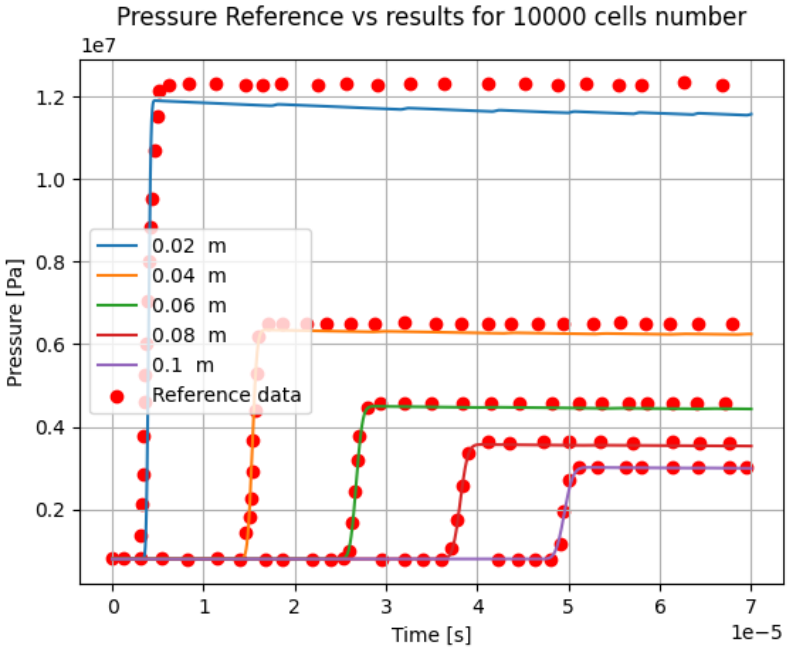

Figure 26: Pressure time evolution at multiple radii: comparison between present results and reference solution (10,000-element mesh).

3.6 Grid convergence study

A grid convergence study was carried out to assess the impact of mesh resolution on the numerical results. Simulations were performed using meshes of 2000, 5000 and 10000 elements, and the results were compared with those reported in [5], obtained with a uniform mesh of 1,000 elements, to evaluate convergence.

The grid convergence analysis showed that numerical diffusion decreases as the mesh is refined. However, to limit computational costs, employing a higher-order spatial reconstruction represents a more efficient approach.

- **Radial pressure results**: in the below, the obtain pressure radial distributions are reported and compared to reference data (figures 27, 28, 29). The decrease in pressure values can be seen to be affected by numerical diffusion, particularly upstream of the shock front.

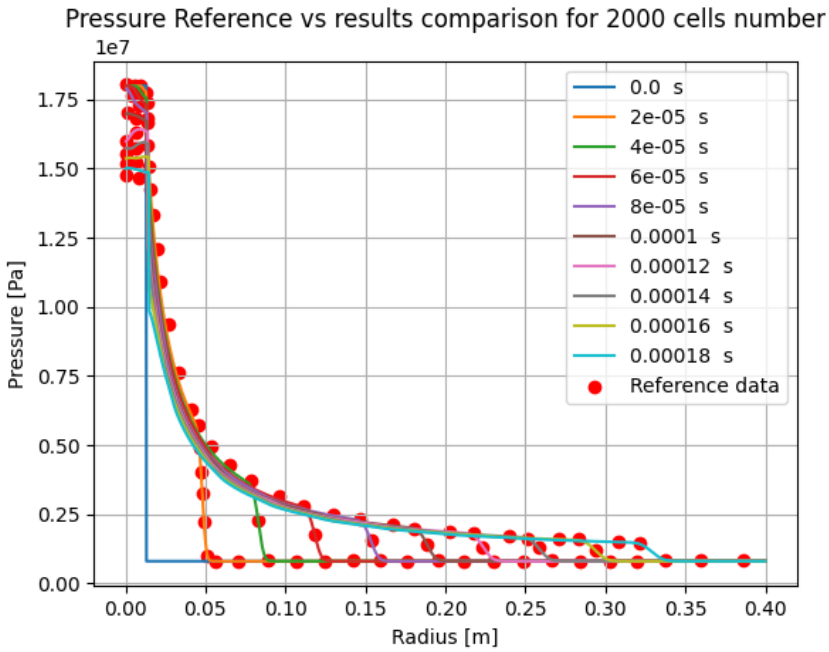

Figure 27: Radial pressure distribution at multiple times: comparison between present results (2,000-element mesh) and reference solution[5].

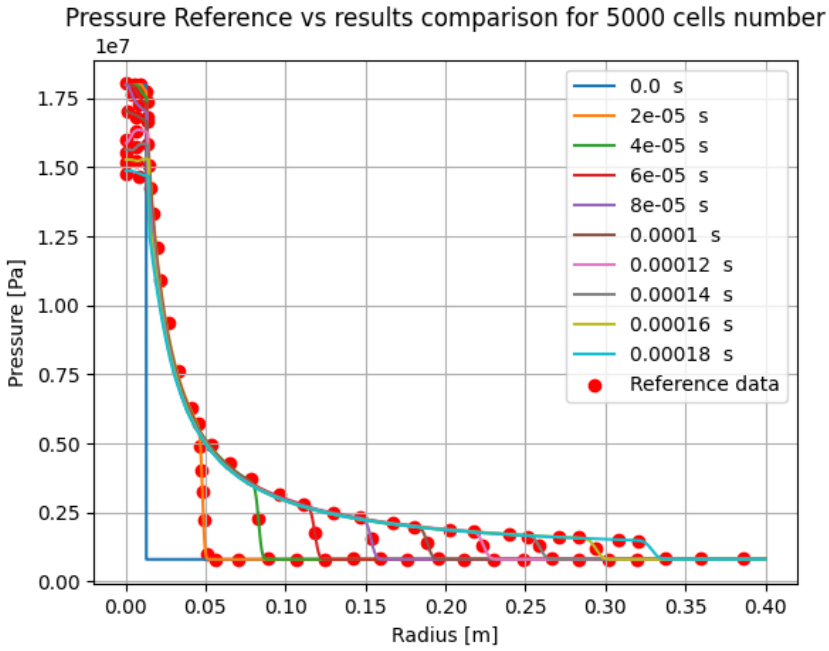

Figure 28: Radial pressure distribution at multiple times: comparison between present results (5,000-element mesh) and reference solution[5].

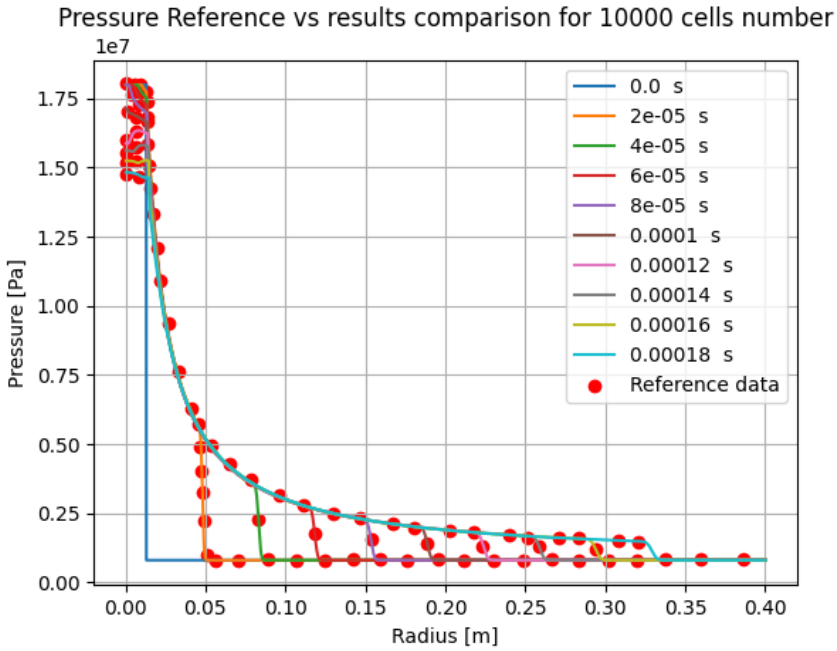

Figure 29: Radial pressure distribution at multiple times: comparison between present results (10,000-element mesh) and reference solution[5].

- **Radial velocity results**: in the below, the obtain velocity radial distributions are reported and compared to reference data (figures 30, 31, 32). As the number of mesh elements increases, the maximum velocity tends to approach the reference value as the numerical diffusion decreases.

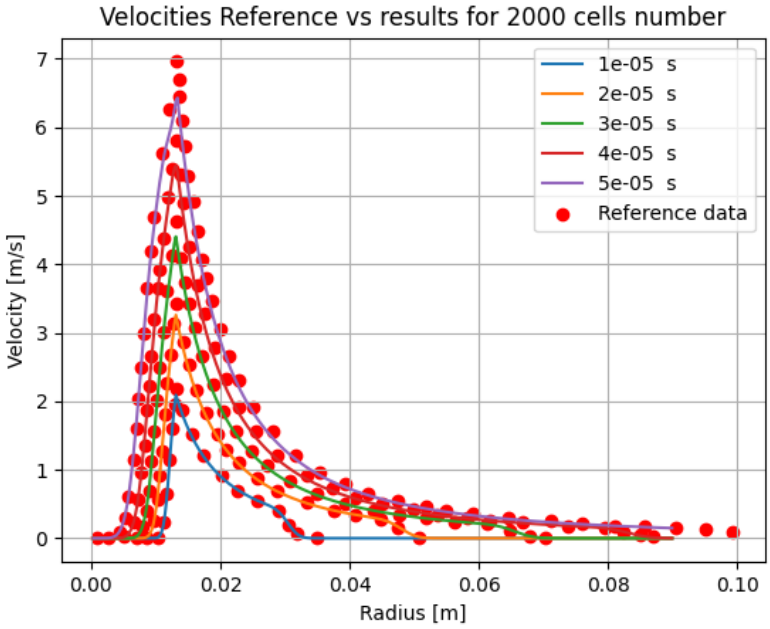

Figure 30: Radial velocity distribution at multiple times: comparison between present results (2,000-element mesh) and reference solution[5].

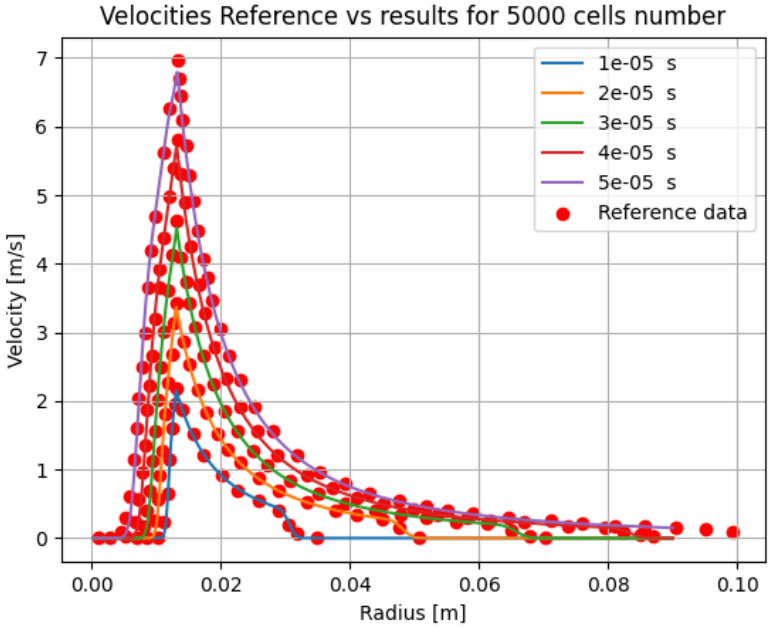

Figure 31: Radial velocity distribution at multiple times: comparison between present results (5,000-element mesh) and reference solution[5].

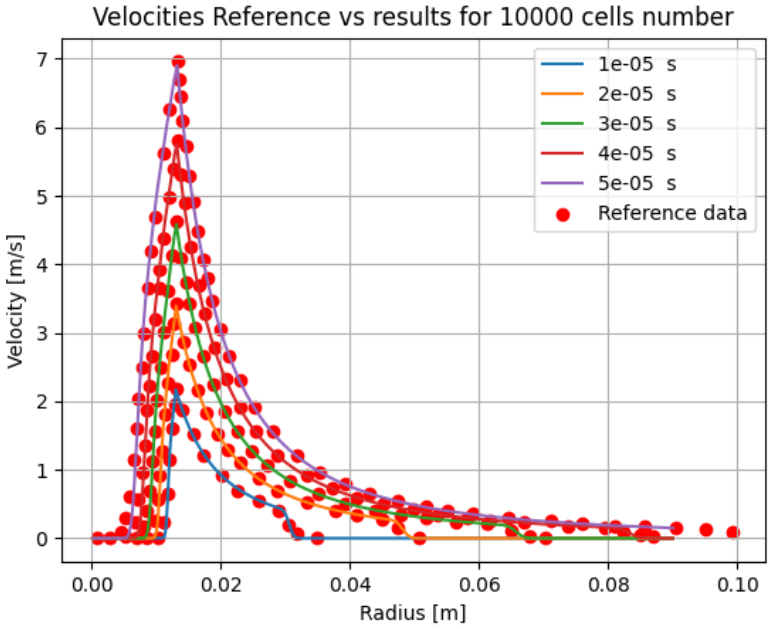

Figure 32: Radial velocity distribution at multiple times: comparison between present results (10,000-element mesh) and reference solution[5].

- **Pressure time evolution results**: in the below, the obtain pressure time evolutions are reported and compared to reference data (figures 33, 34, 35). As aforementioned, numerical diffusion doesn't allow pressure values to remain constant as they should.

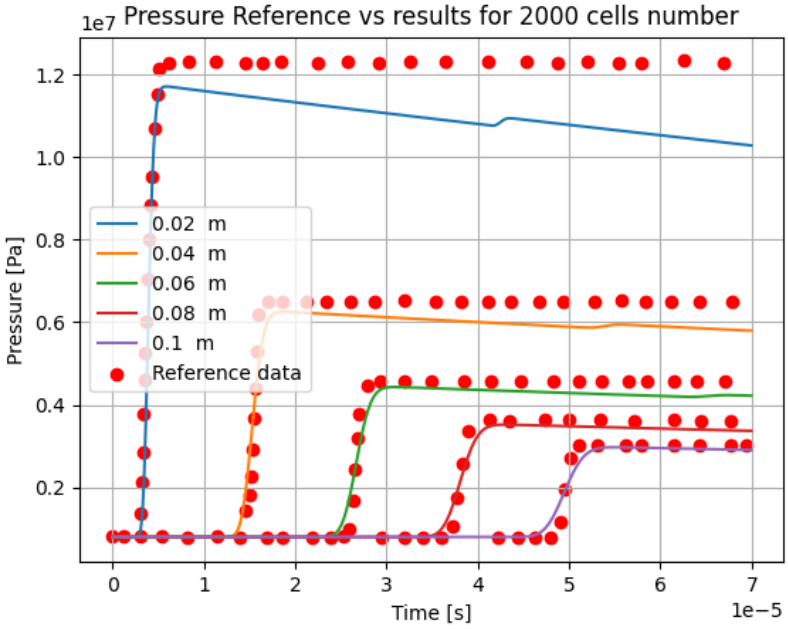

Figure 33: Pressure time evolution at multiple radii: comparison between present results (2,000-element mesh) and reference solution[5].

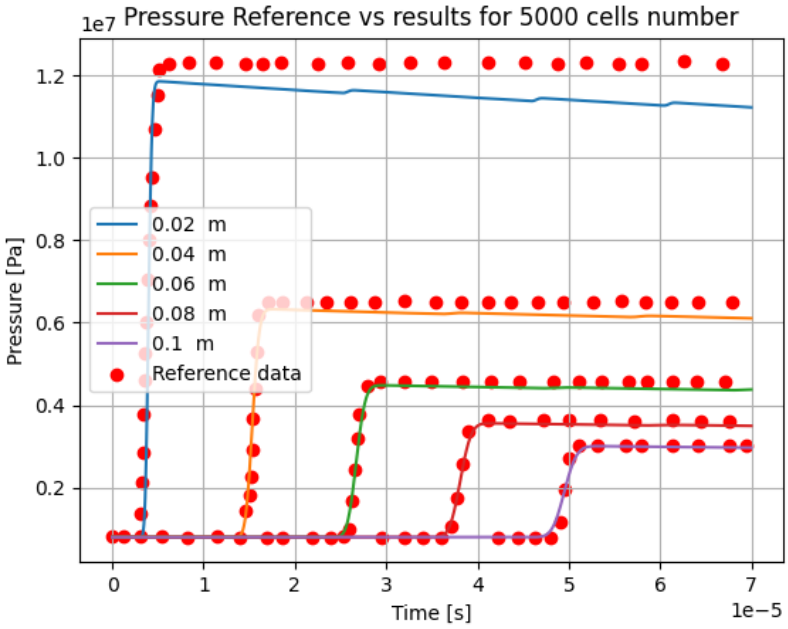

Figure 34: Pressure time evolution at multiple radii: comparison between present results (5,000-element mesh) and reference solution[5].

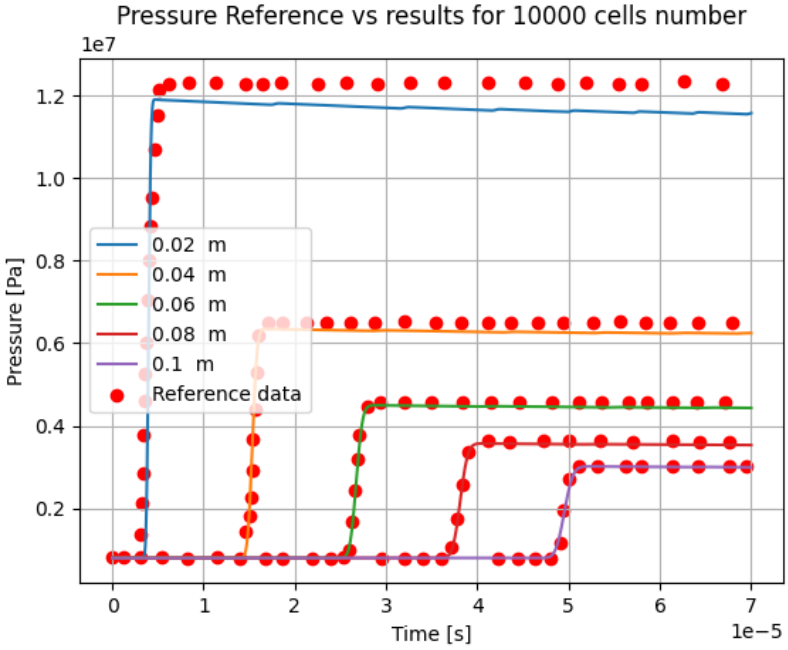

Figure 35: Pressure time evolution at multiple radii: comparison between present results (10,000-element mesh) and reference solution[5].

4 Interface Time Evolution - Hydrodynamic Impact Model

The pressure relief leads to water evaporation and droplet expansion, thus the water-lead interface evolves in time. The Hydrodynamic Impact Model aim is to investigate this phenomenon.

4.1 Problem formulation

Consider an expanding water droplet in the lead pool, leading to lead motion. Due to the high inertia of liquid heavy metal, the droplet expansion results slower that the elastic compression propagation, and can be studied as a subsonic phenomenon. Those consideration leads to the formulation of another mathematical model, proposed in [5] and [6]. This model is particulary useful to investigate the mechanical loads on the reactor walls due to the lead displacement.
The model assumption are the same of the Shock Impact model, adding the following ones:

- The liquid lead is supposed to be incompressible fluid.
- In the water droplet all the thermodynamic properties are volume avereged.

4.2 Mathematical model

The following provides the mathematical modeling of water and lead zones, together with the interface treatment that couples the water and lead descriptions.

4.2.1 Water zone

The water zone is described strating from the mass conservation equation, proposed as:

$$\rho_w R^3 = \text{const} \tag{71}$$

where R is considered to be the water droplet radius and ρ_w the water density. This equation leads to:

$$R_w(t)\frac{d\rho_w(p_w(t))}{dp}\frac{dp_w(t)}{dt} + 3\rho_w(p_w(t))\frac{dR_w(t)}{dt} \tag{72}$$

where p_w is considered to be the water pressure.

4.2.2 Lead zone

The lead zone is described by the incompressible fluid equations in spherical coordinates:

$$\begin{cases} \frac{\partial u_l(r,t)}{\partial t} + 2\frac{u_l(r,t)}{r} = 0 \\ \frac{\partial u_l(r,t)}{\partial t} + u_l(r,t)\frac{\partial u_l(r,t)}{\partial r} + \frac{1}{\rho_l}\frac{\partial p_l(r,t)}{\partial r} = 0 \end{cases} \tag{73}$$

where u_l, ρ_l and p_l are, respectively the lead velocity, density and pressure.

The first equation, and therefore the second one (by substituting and integrating), admits an analitycal solution, as reported in [6]:

$$\begin{cases} u_l(r,t) = \frac{\psi(t)}{r^2} \\ p_l = p_{l0} - \frac{1}{2}\frac{\rho_l \psi^2(t)}{r^4} + \frac{\rho_l}{r}\frac{d\psi(t)}{dt} \end{cases} \tag{74}$$

where $\psi(t)$ is an arbitrary function and $p_{l,0}$ is the initial lead pressure.

4.2.3 Material interface and problem coupling

The considered interface conditions are the physical ones for a contact surface, so the same pressure and velocity are present on both sides of the discontinuity. The interface velocity is thus obtained as:

$$u_l(r,t) = \frac{dR_w(t)}{dt} = V(t) \tag{75}$$

While the pressure interface is derived by $p_l = p_{int} = p_w$ as follows:

$$p_w(R(t),t) = p_l(R(t),t) = p_{l,0} - \rho_l \frac{V^2(t)}{2} + \frac{\rho_l}{R(t)}\frac{d\psi(t)}{dt} \tag{76}$$

By multiplying and dividing by R the last addend, it is possible to write:

$$p_w(R(t),t) = p_l(R(t),t) = p_{l,0} - \rho_l \frac{V^2(t)}{2} + \frac{R(t)\rho_l}{R^2(t)}\frac{d\psi(t)}{dt} \tag{77}$$

And using the derivatives rules:

$$p_w(R(t),t) = p_l(R(t),t) = p_{l,0} - \rho_l \frac{V^2(t)}{2} + \frac{R(t)\rho_l}{R^2(t)}\left[\frac{d}{dt}\frac{\psi(t)}{R^2(t)} - \psi(t)\frac{d}{dt}\frac{1}{R^2(t)}\right] \tag{78}$$

That leads to:

$$\frac{dV(t)}{dt} + \frac{3}{2}\frac{V^2(t)}{R(t)} + \frac{p_{l,0} - p_w}{\rho_l R(t)} = 0 \tag{79}$$

The system is then described by three coupled ODEs:

$$\begin{cases} R_w(t)\frac{d\rho_w(p_w(t))}{dp}\frac{dp_w(t)}{dt} + 3\rho_w(p_w(t))\frac{dR_w(t)}{dt} = 0 \\ \frac{dR_w(t)}{dt} = V(t) \\ \frac{dV(t)}{dt} + \frac{3}{2}\frac{V^2(t)}{R_w(t)} + \frac{p_{l,0} - p_w(t)}{\rho_l R_w(t)} = 0 \end{cases} \tag{80}$$

By solving the above system is possible to obtain the lead radial distributions of pressure and velocity as:

$$\begin{cases} u_l = \frac{R^2(t)}{r^2}V(t) \\ p_l = p_{l,0} - \frac{\rho_l V^2(t)}{2}\frac{R^4(t)}{r^4} + \rho_l \frac{R(t)}{r}\left(2[V^2(t)] + R(t)\frac{dV(t)}{dt}\right) \end{cases} \tag{81}$$

4.3 Numerical implementation and results

The code structure and the obtained results are presented below. Since the model consists of a system of ordinary differential equations (ODEs), no dedicated time-integration solver was developed; instead, a SciPy ODE solver was used [16].

4.3.1 Code structure

The model was implemented in Python using an object-oriented approach and is organized into five classes, as follows:

- **Input class:** Reads an external YAML file defined by the user to initialize the required simulation data.
- **Lead class:** Contains the physical laws governing lead and provides the equations for its radial pressure and velocity distribution.
- **Water class:** Contains the physical laws governing water. Since the closure relations are the same as those used in the SIM model, water properties are obtained through linear interpolation of NIST tabulated data for saturated water [12].
- **Solver class:** Integrates the system of ODEs for water using a SciPy solver.
- **Output class:** Manages all output operations.

4.3.2 Results

The code was run using the same initial conditions as in [6], in order to compare the results of the calculations with those provided.This conditions are the following ones:

- **Initial conditions**:
  - $p_{w,0} = 18.0\,MPa$ or $p_{w,0} = 22.0\,MPa$
  - $\rho_l = 10417.4\,kg/m^3$
  - $p_{l,0} = 0.8\,MPa$
  - $R_{w,0} = 0.013\,m$ or $R_{w,0} = 0.02\,m$
  - $V_0 = 0.0\,m/s$
- **Solver settings**:
  - $t_0 = 0.0s$
  - $t_{end} = 0.035s$
  - Number of timesteps = 1000
  - Numerical scheme = Range-Kutta
  - $R_{max} = 0.5\,m$
  - Cells number = 1000

The plots presented in the paper were digitally sampled and the extracted data was overlaid on the calculation results. These verifications have been performed for both the water-lead interface and the quantities of lead. The red points in the figures below represent the sampled data, while the blue lines represent the code outputs.

Interface results

The interface quantities exhibit some periodicity that is physically unlikely. This is caused by the assumption of inviscid fluids, whereby the droplet is supposed to expand until the increased pressure causes it to contract. Interface test performed:

- Time evolution of interface pressure for an initial water droplet radius of 20mm (figure 36)
- Time evolution of water droplet radius for an initial value of 20mm (Fig. 37)
- Time evolution of interface velocity for an initial water droplet radius of 20mm (Fig. 38)

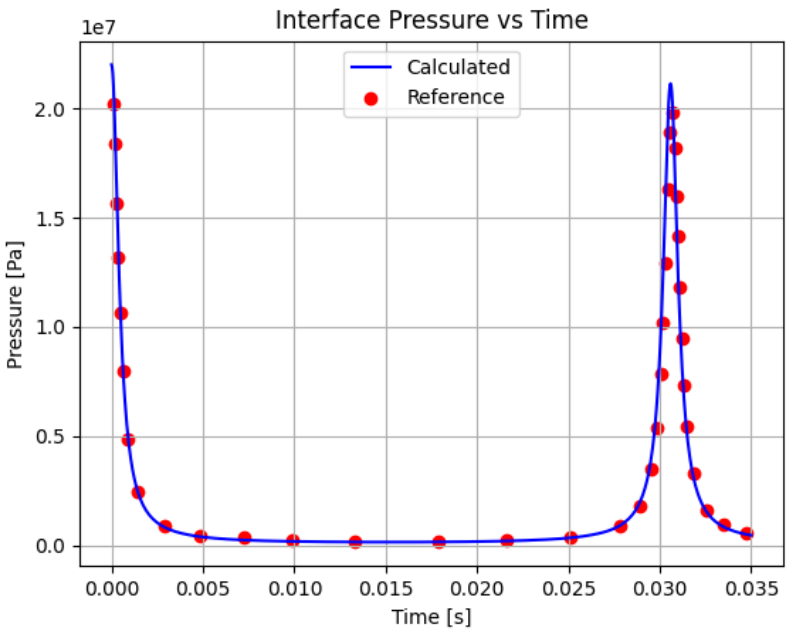

Figure 36: Interface pressure time evolution: results Vs reference.

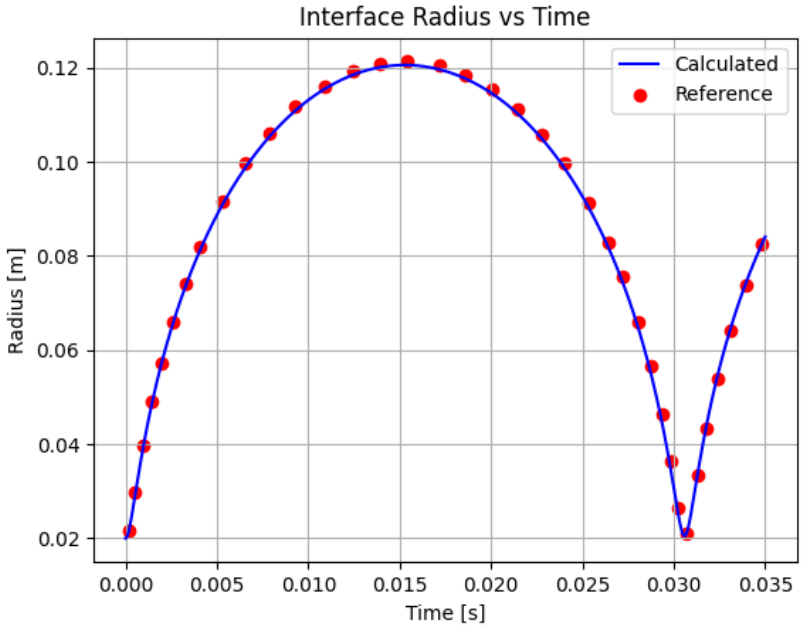

Figure 37: Water droplet radius time evolution: results Vs reference.

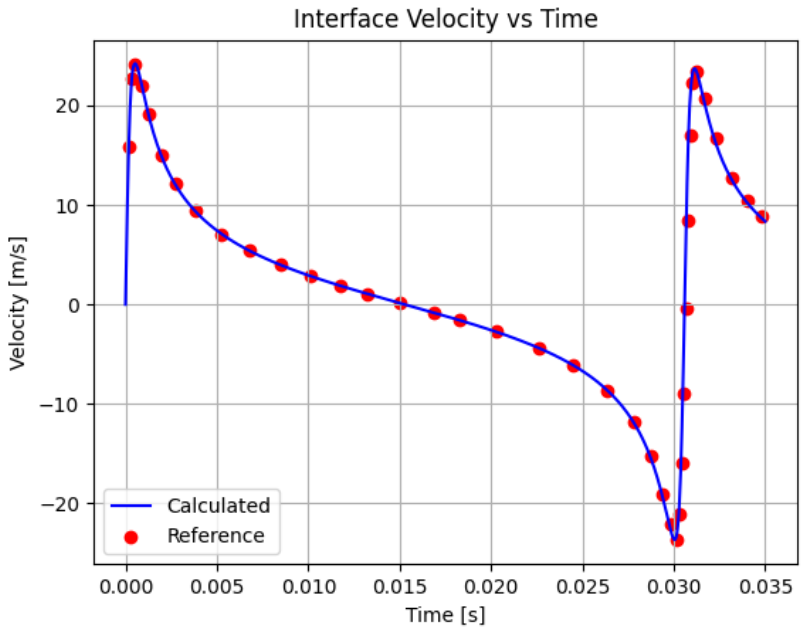

Figure 38: Interface velocity time evolution: results Vs reference.

Lead results

The lead tests highlighted pressure and velocities increasing more near the material interface, as they shoud. This results are also according to the Shock Impact Model caclulations.
Note that the article graphic data of lead distributions were only provided for radial coordinates r such that $r > 2.5\,cm$. The code calculations were plotted from the

first cell of the lead domain instead, so the initial reference data is missing due to that difference.

Lead distributions test performed:

- Lead pressure and velocity radial distributions at 0.04 ms (Fig. 39, 40)
- Lead pressure and velocity radial distributions at 0.08 ms (Fig. 41, 42)

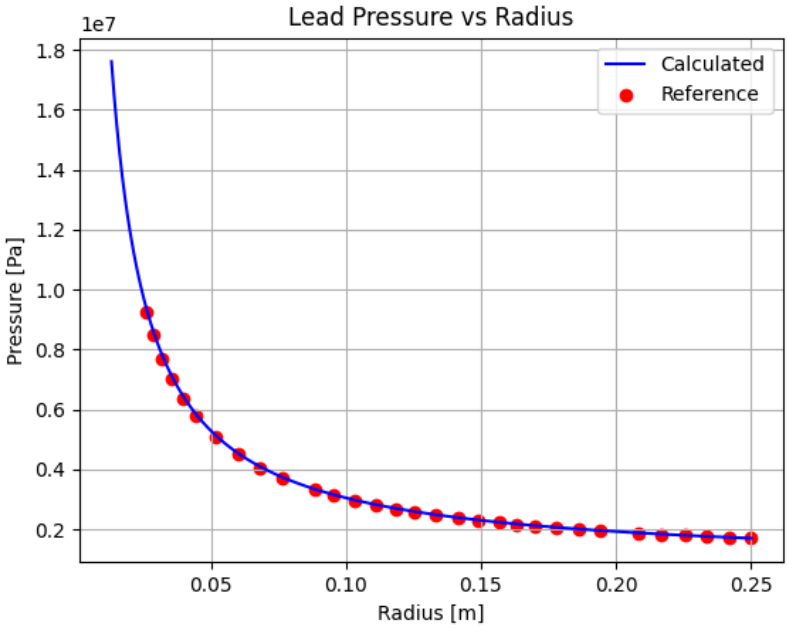

Figure 39: Lead pressure radial distribution at time 0.04 ms.

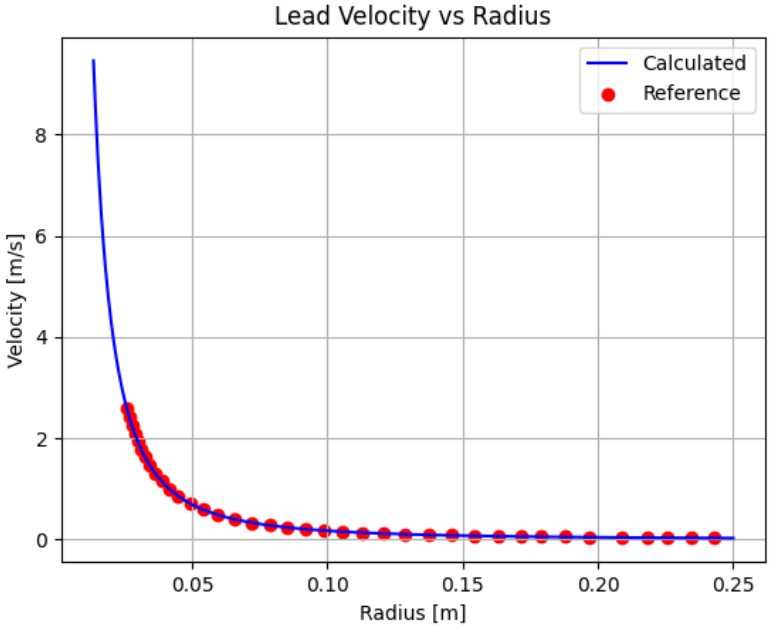

Figure 42: Lead velocity radial distribution at time 0.08 ms.

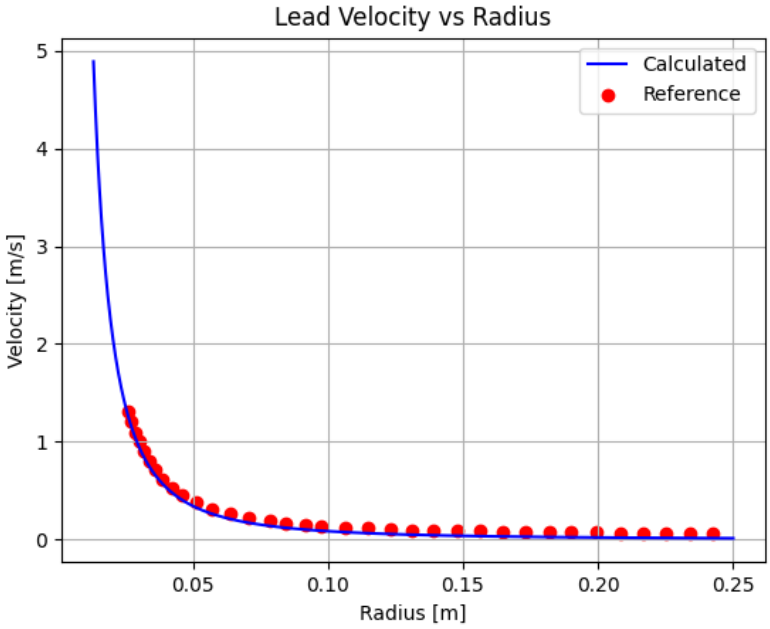

Figure 40: Lead velocity radial distribution at time 0.04 ms.

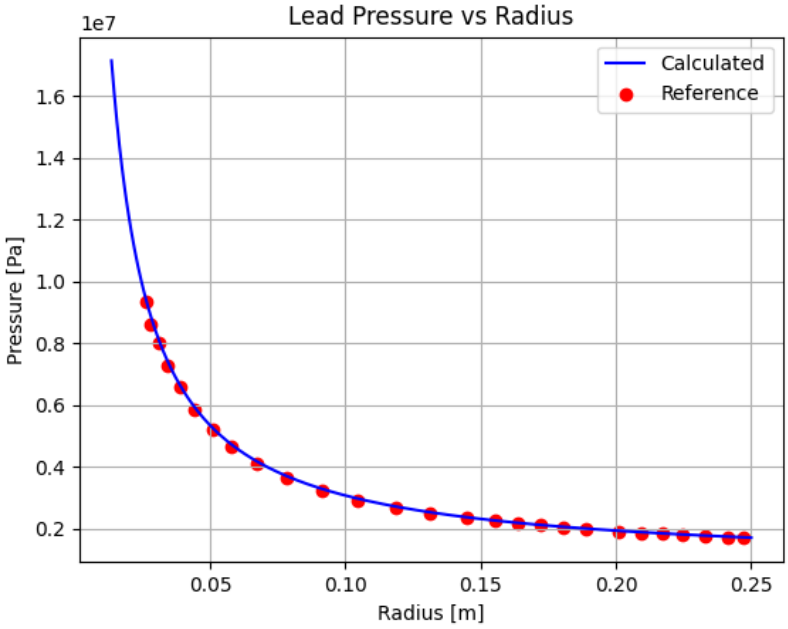

Figure 41: Lead pressure radial distribution at time 0.08 ms.

It is important to note that this model does not consider the impact of shock waves because the lead is assumed to be incompressible. Therefore, the calculation outcomes used to estimate the loads on the reactor walls are only useful for the sloshing initiation phenomenon, which occurs over a longer time period than shock propagation.

5 Conclusions

The Steam Generator Tube Rupture (SGTR) phenomenon represents a relevant accident scenario that must be considered in safety evaluations of Lead-cooled Fast Reactors (LFRs) .

The initiation of shock wave propagation and the time evolution of the water-lead interface were investigated by implementing two models available in the literature. These models describe the behavior of a spherical droplet of high-pressure, saturated water suddenly introduced in a molten lead environment. In the absence of experimental data, the numerical results obtained were compared with those reported in the literature.

A PDE-based solver was implemented for the first model, which captures the rapid propagation of a shock wave through the lead pool. The results showed a sharp decay of the shock intensity and an increase in radial velocity. From a numerical standpoint, the simulations exhibited significant numerical diffusion due to the use of a first-order reconstruction, which decreases linearly with increasing grid resolution. Employing a higher-order spatial reconstruction would reduce numerical diffusion with only a modest increase in computational cost and should therefore be considered in future studies.

The second model was solved using an existing ODE solver, and the results were in good agreement with to those available in the literature. The droplet dynamics display a non-physical periodicity due to the inviscid-fluid assumption, but the lead velocity and pressure distributions are consistent with the outcomes of the first model.

These results obtained in this work can serve as a basis for assessing the potential mechanical damage to reactor structures in an SGTR event. Moreover, the developed numerical tools can support safety evaluations for Lead-cooled Fast Reactors.

References

[1] Truc-Nam Dinh. "Multiphase flow phenomena of steam generator tube rupture in a lead-cooled reactor system: a scoping analysis". In: *Proceedings of ICAPP*. Vol. 13. 2007, p. 7497.

[2] Qifan Yu et al. "An experimental review of steam generator tube rupture accident in lead-cooled fast reactors: Thermal-hydraulic experiments classification and methods introduction". In: *Progress in Nuclear Energy* 160 (2023), p. 104711.

[3] W. Maschek et al. *The SIMMER Safety Code System and its Validation Efforts for Fast Reactor Application*. Paul Scherrer Institut - PSI, 2008.

[4] Europlexus Team and Pascal Galon. *Europlexus: a computer program for the finite element simulation of fluid-structure systems under transient dynamic loading. User's manual*. Feb. 2016.

[5] SE Yakush et al. "Pressure waves due to rapid evaporation of water droplet in liquid lead coolant". In: *Science and Technology of Nuclear Installations* 2018.1 (2018), p. 3087051.

[6] AS Iskhakov et al. "Steam generator tube rupture in lead-cooled fast reactors: estimation of impact on neighboring tubes". In: *Nuclear Engineering and Design* 341 (2019), pp. 198–208.

[7] AS Iskhakov et al. "Hugoniot analysis of experimental data on steam explosion in stratified melt-coolant configuration". In: *Nuclear Engineering and Design* 347 (2019), pp. 151–157.

[8] AV Kapustin et al. "Thermal detonation wave in liquid lead–water mixture". In: *Journal of Physics: Conference Series*. Vol. 2088. 1. IOP Publishing. 2021, p. 012027.

[9] Vladimir Melikhov, Oleg Melikhov, and Bashar Saleh. "Calculation of stationary thermal detonation wave in the multiphase system "water drops, surrounded by steam films, in continuous molten lead"". In: *E3S Web of Conferences*. Vol. 459. EDP Sciences. 2023, p. 04010.

[10] SJ Board, RW Hall, and RS Hall. "Detonation of fuel coolant explosions". In: *Nature* 254.5498 (1975), pp. 319–321.

[11] Xiang Yu Hu and Boo Cheong Khoo. "An interface interaction method for compressible multifluids". In: *Journal of Computational Physics* 198.1 (2004), pp. 35–64.

[12] National Institute of Standards and Technology. *NIST Chemistry WebBook*. 2025. URL: `https://webbook.nist.gov/chemistry/`.

[13] Concetta Fazio et al. *Handbook on lead-bismuth eutectic alloy and lead properties, materials compatibility, thermal-hydraulics and technologies-2015 edition*. Tech. rep. Organisation for Economic Co-Operation and Development, Nuclear Energy ..., 2015.

[14] Eleuterio F Toro. *Riemann solvers and numerical methods for fluid dynamics: a practical introduction*. Springer Science & Business Media, 2013.

[15] Ronald P Fedkiw et al. “A non-oscillatory Eulerian approach to interfaces in multimaterial flows (the ghost fluid method)”. In: *Journal of computational physics* 152.2 (1999), pp. 457–492.

[16] Pauli Virtanen et al. “SciPy 1.0: Fundamental Algorithms for Scientific Computing in Python”. In: *Nature Methods* 17 (2020), pp. 261–272. DOI: 10.1038/s41592-019-0686-2.